

Large Area Mapping at 850 Microns. V. Analysis of the Clump Distribution in the Orion A South Molecular Cloud

Doug Johnstone^{1,2} & John Bally³

ABSTRACT

We present results from a 2300 arcmin² survey of the Orion A molecular cloud at 450 and 850 μm using the Submillimetre Common-User Bolometer Array (SCUBA) on the James Clerk Maxwell Telescope. The region mapped lies directly south of the OMC1 cloud core and includes OMC4, OMC5, HH1/2, HH34, and L1641N. We identify 71 independent clumps in the 850 μm map and compute size, flux, and degree of central concentration in each. Comparison with isothermal, pressure-confined, self-gravitating Bonnor-Ebert spheres implies that the clumps have internal temperatures $T_d \sim 22 \pm 5$ K and surface pressures $\log(k^{-1} P \text{ cm}^{-3} \text{ K}) = 6.0 \pm 0.2$. The clump masses span the range 0.3 – 22 M_\odot assuming a dust temperature $T_d \sim 20$ K and a dust emissivity $\kappa_{850} = 0.02 \text{ cm}^2 \text{ g}^{-1}$. The distribution of clump masses is well characterized by a power-law $N(M) \propto M^{-\alpha}$ with $\alpha = 2.0 \pm 0.5$ for $M > 3.0 M_\odot$, indicating a clump mass function steeper than the stellar Initial Mass Function. Significant incompleteness makes determination of the slope at lower masses difficult. A comparison of the submillimeter emission map with an H₂ 2.122 μm survey of the same region is performed. Several new Class 0 sources are revealed and a correlation is found between both the column density and degree of concentration of the submillimeter sources and the likelihood of coincident H₂ shock emission.

Subject headings: infrared: ISM: continuum - ISM: individual (OMC4, OMC5, HH1/2, HH34, L1641N, Orion A South) - ISM: structure - stars: formation

¹National Research Council Canada, Herzberg Institute of Astrophysics, 5071 West Saanich Rd, Victoria, BC, V9E 2E7, Canada; doug.johnstone@nrc-cnrc.gc.ca

²Department of Physics & Astronomy, University of Victoria, Victoria, BC, V8P 1A1, Canada

³Center for Astrophysics and Space Astronomy and Department of Astrophysical and Planetary Sciences, University of Colorado, Boulder, CO 80309; bally@casa.colorado.edu

1. Introduction

Star formation takes place within molecular clouds, in regions where the local pull of gravity overwhelms the random and ordered motions of the gas. Thus, in order to understand the physical process of star formation it is necessary to observe the formation and evolution of structure inside these clouds. The advent of sensitive millimeter and submillimeter continuum array detectors has provided an opportunity for large area mapping of the optically thin emission from cold dust within molecular clouds, yielding observations of the column density distribution within these regions. The most common features observed in these maps are dense condensations of dust, “clumps”¹. These clumps reside in areas where stars are either forming or are expected to form. When combined with observations being taken at shorter wavelengths by the Spitzer Space Telescope, it should be possible to unambiguously classify these objects as either starless (possibly prestellar) or protostellar (Class 0 or Class I) (Jorgensen et al. 2006). Alternatively, comparison with other evolutionary tracers, such as H₂ shock emission (Walawender et al. 2005, 2006), provides evidence for which clumps already contain forming stars.

Continuing an effort to quantify the necessary pre-conditions for star formation, and in anticipation of the Spitzer observations, in this paper we present submillimeter dust continuum maps of the Orion A South region, including OMC4, OMC5, HH1/2, HH34, and L1641N. Previous papers in the series investigated the northern portion of the Orion A cloud containing the Orion Nebula (Johnstone & Bally 1999), the Ophiuchus cloud (Johnstone et al. 2000b, hereafter Paper II), the Orion B North region (Johnstone et al. 2001, hereafter Paper III), and the Orion B South region (Johnstone, Matthews, & Mitchell 2006, hereafter Paper IV).

The Orion A molecular cloud south of the Orion Nebula contains several active sites of ongoing star and star cluster formation. The region dubbed OMC4 is located about 10′ south of the Orion Nebula and consists of a V-shaped cluster of cores located near the top portion of the SCUBA survey. The double star ι Orionis (spectral types O9III, B1III), about 30′ south of the Orion Nebula, is the brightest member of the >3 Myr old NGC 1980 cluster located in the southern part of the Integral Shaped Filament (ISF) in Orion A. The ι Orionis system has been implicated in a four-body dynamical interaction that launched the famous high-velocity run-away stars AE Auriga and μ Columbae 2.6 Myr ago (Hoogerwerf, de Bruijne, & de Zeeuw 2001). This portion of the Orion OB1c association must lie at least

¹Unfortunately, the words “cores” and “clumps” have ambiguous meaning and are used to denote various types of objects by different authors. In this paper “clumps” refer to stellar-mass sized condensations of dust and gas.

10 pc in front of the Orion A cloud and must represent a considerably older site of star birth than either the Orion Nebula or the other currently active star forming regions in Orion A (Brown et al. 1994).

The embedded L1641N cluster contains at least 30 mid-infrared sources detected by ISO (Ali & Noriega-Crespo 2004; Chen & Tokunaga 1994). Young stars in this cluster power dozens of Herbig-Haro (HH) flows, including two giant flows that can be traced for several parsecs from the L1641 cluster core (Reipurth, Devine, & Bally 1998). The L1641N cluster is the most active site of on-going star formation in the fields covered by this SCUBA survey.

The western side of the Orion A cloud near the L1641N cluster contains a number of Herbig-Haro objects and young stars not associated with rich clusters. The HH 34 jet, located about 16' west of the L1641 region, emerges from a star embedded within a small cloud which hosts a small group of young stars (e.g. Devine et. al. 1997). The source and true nature of the bright but enigmatic bow-shaped HH 222, located about 5' north-northwest of HH 34, remains unknown (Castets, Reipurth, & Loinard, 2004). However, another giant bow, HH 401, located about 5' southwest of HH 34 appears to trace a parsec-scale outflow possibly powered by the HH 1/2 jet (Ogura 1995).

Near the southern periphery, our survey field contains the bright NGC1999 reflection nebula and its exciting star V380 Ori (spectral type A0e). Many molecular outflows and Herbig-Haro objects are observed here, suggesting that this region also contains a small embedded group of young stars (Chen & Tokunaga 1994). NGC1999 is associated with a dense cloud core and molecular ridge, seen in millimeter CO and CS transitions, which extends about 10' towards the south (Morgan et al. 1991). The southern end of this ridge contains the famous Herbig-Haro objects HH 1, 2, and 3, as well as a number of fainter shocks (e.g. HH 144/145 and HH 147). This region contains another compact group of young stars.

2. Observations and Data Reduction

The data covering the Orion A South region were obtained between 1997 and 2002 using SCUBA at the JCMT. The JCMT archive hosted by the CADC² was used to find all relevant observations toward the region. A total of 305 individual scan-maps, each approximately 100

²Extensive use of the JCMT archive at the Canadian Astronomy Data Centre (CADC) was used to retrieve all relevant SCUBA data in Orion A South. The CADC is operated by the Dominion Astrophysical Observatory for the National Research Council of Canada's Herzberg Institute of Astrophysics.

arcmin², were obtained, covering a combined 2300 square arcminute region. Each individual 3-arcsecond cell in the map was measured approximately 40 times at 850 μm and 90 times at 450 μm . Thus, the total time spent observing each cell was approximately 5 and 11 seconds respectively. The weather conditions varied significantly during the many nights of observing, especially at 450 μm . The mean and deviation of the optical depths at 850 μm were $\tau_{850} = 0.26 \pm 0.10$ and at 450 μm were $\tau_{450} = 1.1 \pm 0.3$.

The raw bolometer data were reduced using the standard SCUBA software (Holland et al. 1999) to flat-field, extinction-correct, and flux calibrate. The extinction corrections, which provide atmospheric optical depth corrections, and flux calibrations as a function of time were obtained from the JCMT calibrations archive (Jenness et al. 2002). The extinction corrections are tabulated as a function of time based on a comparison of skydip measurements taken with the JCMT during normal observing and zenith optical depth measures taken every few minutes at 225 GHz by the CSO tau meter. The flux calibration values are tabulated from all calibration measurements taken during extended periods of time, e.g. semesters, over which the telescope and instrument were not known to have changed significantly (Jenness et al. 2002). Typical uncertainties in the flux calibration can be determined from Jenness et al. (2002; their Figures 1 and 2). At 850 μm the uncertainty is approximately $\pm 10\%$ while at 450 μm the uncertainty is closer to $\pm 25\%$. These values are consistent with the uncertainties determined by individual observers using calibrator sources. Most of the uncertainty is caused by changes in the telescope surface due to temperature and gravity during the night and resultant changes in the beam profile, which can be quite significant at 450 μm . In addition, the beam profiles are not entirely Gaussian, resulting in complications when attempting to determine total flux measurements for extended objects. At 450 μm this is a rather severe problem as a significant portion of the total flux is contained in the broader error beam.

The data were further reduced and transformed into the final maps using the matrix inversion technique discussed by Johnstone et al. (2000a, hereafter Paper I). This inversion technique has many advantages, in particular the ability to utilize *all* data taken with SCUBA at the JCMT, regardless of the observing method (i.e. arbitrary chop throws and chop directions) and to properly weight each observation by the noise inherent in the individual bolometer. Significant low-amplitude, large-scale features remain after the image reconstruction. Although these features may be real, artificial structure on these scales are often produced by weather variations and bolometer drift since reconstruction of chopped data amplifies long spatial wavelength noise. To filter these features, the map was convolved with a large Gaussian ($\sigma = 135''$) and the resultant smoothed map was subtracted from the reconstruction. In order to minimize the effect of over-subtraction in regions with bright sources, all pixels greater than 0.25 Jy bm^{-1} at 850 μm and 5 Jy bm^{-1} at 450 μm were

removed in the construction of the smoothed map. The final, reconstructed $850\ \mu\text{m}$ and $450\ \mu\text{m}$ maps, after filtering, are shown in Figure 1 along with maps of the estimated uncertainty at each position. Figure 2 shows blow ups of the four most interesting regions. Note that the uncertainty in the measurement drops significantly in regions where multiple observations were obtained. Although the noise in the final reconstructed maps is not uniform across the image, the typical value per $3''$ pixel is $0.03\ \text{Jy}\ \text{bm}^{-1}$ at $850\ \mu\text{m}$ and $0.3\ \text{Jy}\ \text{bm}^{-1}$ at $450\ \mu\text{m}$.

3. Data Analysis: Clump Properties in Orion A South

3.1. Identification of Clumps

Clumps within the Orion A South region were identified in the same manner used for Ophiuchus (Paper II), Orion B North (Paper III), and Orion B South (Paper IV), allowing for a direct comparison of the results. Briefly, the clump finding algorithm, `clfind` (Williams et al. 1994), was employed to determine the location and extent of individual clumps. This technique separates the map into individual clumps by searching for local minima boundaries. Each pixel, above a limiting threshold, is assigned to a particular clump. Thus, unlike Gaussian clump-finding algorithms, the regularity of the clump is not preset and clumps are allowed to have arbitrary shape. We remind the reader that any clump finding algorithm introduces biases into the results through its assumption of what constitutes an individual source; however, by applying the same technique to an ensemble of regions, observed under similar conditions, we intend to use the results of the analysis to highlight the similarities and differences between star-forming regions. Thus, the exact nature of the clump finding algorithm, although important for understanding the details of the objects which it identifies, is not critical. We prefer `clfind` over other techniques, such as Gaussian-profile clump finding algorithms (Stutzki & Güsten 1990), explicitly because it does not prejudge the degree of isotropy of each region.

Initially 83 clumps were obtained by the `clfind` routine; however, 12 were removed on visual inspection of the clump location and the Orion A South map. All clumps removed were near the edge of the map where the residual noise is highest. Following the earlier papers in this series, the effective radius of each clump was determined by taking the total area enclosed within the clump boundary and computing the radius of a circle required to reproduce the result. The properties of the 71 identified clumps are presented in Table 1. The total flux for each clump has not been corrected for the effect of the telescope error beam, in keeping with previous papers in this series. The error beam at $850\ \mu\text{m}$ is at most $\sim 10\%$, similar to the calibration uncertainties and thus the uncertainty in the final derived

total flux is less than 20%. Figure 3 overlays circles on the Orion A South map with the central location marking the measured center of each clump and the circle size a measure of the extent of the clump. It is clear from visual inspection that in a few crowded regions the measured clumps are asymmetric and may be composite objects.

The mass for each clump was estimated by calculating the total flux from within the clump boundary and assuming that the measured flux was due to thermal emission from optically thin dust particles. As in Paper IV, the opacity per unit mass column density at $\lambda = 850 \mu\text{m}$ was taken to be $\kappa_{850} = 0.02 \text{ cm}^2 \text{ g}^{-1}$. This value is larger than the value used in Papers II and III, thus lowering the mass determination for a fixed total flux, but reflects a consensus view that the dust in dense regions has a higher emissivity at long wavelengths (van der Tak et al. 1999). We remind the reader that the value of κ depends sensitively on the properties of the dust grains (see Henning, Michel, & Stognienko 1995 for a review). It is also possible for the continuum flux to be contaminated by CO 3–2 emission; however, as shown by Johnstone et al. (2003) this is not typically a concern within nearby star-forming regions since the CO emission line needs to be both strong *and* extremely broad.

Taking the distance to Orion A South to be $d = 450 \text{ pc}$ the flux enclosed within the clump boundary S_{850} , measured in Janskys, is converted to mass via

$$M_{\text{clump}} = 0.75 \times S_{850} \left[\exp\left(\frac{17 \text{ K}}{T_d}\right) - 1 \right] \left(\frac{\kappa_{850}}{0.02 \text{ cm}^2 \text{ g}^{-1}} \right)^{-1} M_{\odot}. \quad (1)$$

Anticipating the results below, the dust temperature is estimated to be $T_d = 20 \text{ K}$. Thus, the measured masses in Orion A South range from $0.3 M_{\odot}$ to $22 M_{\odot}$. The mass versus size relation for the clumps is plotted in Figure 4.

3.2. Modeling Clumps as Bonnor-Ebert Spheres

In order to better estimate the clump properties, such as temperature and mass, and the environment in which the clumps are embedded, it is useful to equate the observed clumps with simple physical constructions. The simplest static models are spherical, isothermal, self-gravitating pressure-confined clumps known as Bonnor-Ebert spheres (Ebert 1955, Bonnor 1956, Hartmann 1998), a one-dimensional family of equilibrium structures equating the importance of self-gravity, and possible collapse, to the degree of central concentration within the clump. In Paper II we developed a technique for identifying the internal clump temperature, the clump mass, and the confining surface pressure on the clump, from the total flux at $850 \mu\text{m}$, S_{850} , the observed size of the clump in arcseconds, (R''_{eff}) , and the concentration, C , of the clump. Given the FWHM beamsizes, B'' , of the observations, and the peak surface

brightness, F_{850} in Jy/beam, the concentration is defined as

$$C = 1 - \frac{1.13 B''^2 S_{850}}{\pi R''_{\text{eff}}^2 F_{850}}. \quad (2)$$

For equilibrium Bonnor-Ebert spheres, the concentration ranges from $C = 0.33$ for uniform density, non-self-gravitating objects to $C = 0.72$ for critically self-gravitating objects. It is important to note that C is an observationally determined quantity and thus depends on both the resolution and sensitivity of the instrument used. Additionally, the manner in which the objects are identified (Gaussian, wavelet, or `clfind`) will affect the measured concentration. Recent findings that the concentration correlates with the existence of an embedded protostar (Walawender et al. 2005, 2006; Jorgensen et al. 2006) has focused interest on this quantity and comparison between the different object identification techniques is being investigated. For further discussion on the complications of this procedure, refer to Papers II, III, and IV.

The concentration of each observed clump is plotted in Figure 5 against both the clump mass, assuming $T_d = 20$ K, and the clump size. Five clumps appear more concentrated than allowed for by Bonnor-Ebert spheres and are flagged by diamonds while three clumps are not concentrated enough to be Bonnor-Ebert spheres and are flagged by crosses. These latter clumps all have relatively low peak brightnesses and lie near bright sources. Thus, their size is likely somewhat confused.

Applying the Bonnor-Ebert sphere analysis used in Papers II-IV, the physical conditions obtained for each clump are plotted in Figure 6. In Paper IV we argue that the internal pressure of the clump is composed of equal contributions from thermal and non-thermal motions and that the opacity is higher than was used in Papers II and III. Combined, these two changes produce almost identical values for clump masses and bounding pressures as was found using the assumptions given in Papers II and III but lower the derived temperatures by a factor of approximately two. Figure 6 plots the external pressure versus the internal temperature for the clumps identified in this paper. We find that the clump temperatures in Orion A are clustered around $T_d = 22 \pm 5$ K. This result is very similar to the values obtained for Orion B South (Paper IV) and Orion B North (Paper III - after accounting for changes in the values used for opacity and pressure support determination). The external pressure required to confine the clumps is $\log(k^{-1} P \text{ cm}^3 \text{ K}^{-1}) = 6.0 \pm 0.2$, similar to that needed in Orion B (Papers III and IV), and a factor of three to ten lower than obtained for the much denser core of Ophiuchus. As discussed in Paper III, this pressure lies within the range expected deep inside the Orion cloud.

3.3. Clump Temperatures Derived From Submillimeter Colors

Comparison of the 850 μm and 450 μm SCUBA maps allows for an independent measure of the dust temperature. The dust temperature within each clump can be estimated from the submillimeter spectral index, γ , where $S(\nu) \propto \nu^\gamma$. Assuming that the dust emission is approximated by a radiating blackbody at temperature T_d and with an opacity $\kappa(\nu)$ which follows a power-law such that $\kappa(\nu) \propto \nu^\beta$, then

$$S(\nu) \propto \nu^\beta B_\nu(T_d), \quad (3)$$

which can be inverted to find T_d from observations of $S(\nu)$. Unfortunately, this technique requires knowledge of β which has been shown to vary significantly with environment (Goldsmith, Bergin, & Lis 1997; Visser et al. 1998; Hogerheijde & Sandell 2000; Beuther, Schilke, & Wyrowski 2004). Friesen et al. (2005) have shown that it is possible to use a Fourier Transform Spectrometer at submillimeter wavelengths to measure β directly, however, present instruments only allow for observations of extremely bright sources.

An additional complication for utilizing multi-wavelength observations to estimate the dust temperature is that the beam size and shape can vary significantly. This is especially acute when using 850 μm and 450 μm observations taken at the JCMT (Hogerheijde & Sandell 2000). The 450 μm beam is poorly approximated by a single Gaussian component, with almost half the flux associated with a broad component about 30'' in extent. Thus, simple attempts to convolve the 450 μm map with a single Gaussian to obtain the lower spatial resolution of the 850 μm map tends to overestimate the contribution of 450 μm emission on large spatial scales. Reid and Wilson (2005) propose a more complicated but accurate approach in which both the maps are convolved with the complex telescope beam profile of the other wavelength. Here we simplify the technique somewhat by taking the typical beam profile at each wavelength, as was performed in Paper IV. Thus, the JCMT 450 μm beam is modeled as two Gaussians with 8.5'' and 30'' FWHM and relative peak intensities of 0.95 and 0.05 while the 850 μm beam is modeled as two Gaussians with 14.5'' and 30'' FWHM and relative peak intensities of 0.95 and 0.05. The fluxes measured and tabulated in Table 2 are derived after convolution and using exactly the same pixels to define each clump in both maps.

Assuming that $\beta = 2$, the dust temperature at the center of each clump is estimated using the total flux in the convolved 850 μm and 450 μm maps. For those sources where the flux ratio produces unphysical temperatures, a value of 50 K is assumed. Unphysical values are caused by the 450 μm to 850 μm ratio becoming larger than a critical value and suggest that either $\beta > 2$ or the 450 μm data is corrupted by contamination by nearby sources or poor flux calibration. We note that the typical uncertainty in the flux calibration is 10% at 850 μm

and 25% at $450\ \mu\text{m}$ (Jenness et al. 2002) which leads to a large uncertainty in the flux ratio and hence the derived submillimeter temperature. The typical dust temperature derived from the submillimeter color measurement is $T_d = 18 \pm 9\ \text{K}$, excluding the sources with unphysical values, in reasonable agreement with the Bonnor-Ebert temperatures. Table 2 catalogues the derived submillimeter spectral index derived temperatures along with the Bonnor-Ebert values. A graphical comparison is presented in Figure 7. There is no clear trend between the two temperature derivations, rather the temperatures appear to be scattered randomly within the bounds of the uncertainty in each measure. This result is consistent with the analysis of Orion B South (Paper IV).

3.4. The Clump Mass Distribution Function

The distribution of clump masses is most easily investigated by plotting the cumulative number $N(M)$ of clumps with masses greater than M . Figure 8 presents the observed clump cumulative mass function for both a constant flux-to-mass ratio ($T = 20\ \text{K}$; thin line) and for masses calculated using the Bonnor-Ebert sphere analysis (thick line). To represent the data with simple power-law fits, $N(M) \propto M^{-\alpha}$, requires $\alpha \sim 2.0 \pm 0.5$ for moderate mass clumps ($M > 3M_\odot$), while the lower mass clumps are well represented by $\alpha \sim 0.5$ (the Salpeter IMF has a slope of $\alpha = 1.35$ in this representation). We stress that incompleteness may be important at the low mass end, biasing α to lower values (c.f. Figure 4 and discussion in Paper II).

The results of this analysis are somewhat inconsistent with those in Papers II-IV as well as the work of other submillimeter data sets obtained in nearby molecular clouds (Motte et al. 1998; Testi & Sargent 1998; Motte et al. 2001). Typically, the continuum clump mass distribution has been comparable to the stellar Initial Mass Function (Scalo 1986; Kroupa et al. 1993; Kroupa 2002), at least for the more massive clumps observed. In Orion A South, however, the clump mass distribution appears *steeper* than the stellar Initial Mass Function, similar to the results of Reid & Wilson (2005). Note that all the observed submillimeter continuum clump mass distributions are significantly steeper, at least at the high mass end, than the distribution of mass inside molecular clouds obtained from CO measurements (Williams & McKee 1997; McKee & Williams 1997; Kramer et al. 1998; Williams, Blitz, & McKee 2000 and references therein).

It is possible that the steep mass function of clumps is related to the steep mass function of stars. In both cases, the majority of mass is accounted for by small objects, unlike the molecular cloud distribution where the rare massive clouds account for the majority of the mass. Perhaps then the mass function of stars is determined before collapse occurs. Only

a small fraction, of order a few percent, of the cloud mass is observed to be in measured submillimeter clumps (Johnstone, Di Francesco, & Kirk 2004; Kirk, Johnstone, Di Francesco 2006), roughly consistent with the overall star formation efficiency in clouds. In contrast, the molecular gas distribution inside clouds, observed in CO, contains the bulk of the cloud mass and is therefore tracing the large-scale complexity of the cloud. When higher density tracers are observed the gas mass fraction is found to be similar to that of the submillimeter clumps, for example H^{13}CO line emission (Onishi et al. 2002). As well, some observations of more distant molecular clouds detect larger, more massive, submillimeter clumps that are observed to have a distribution similar to the CO observations (Kerton et al. 2001; Mookerjee et al. 2004). These results suggest that there is a significant change in the structure of a molecular cloud on small, dense, scales and that the process which drives the formation of these entities is different from the mechanism which produces the large scale structure in clouds.

4. Clump Locations and Comparison with H_2

The mapped portion of Orion A contains several active centers of star formation which are spawning small clusters of stars, including OMC4, OMC5, L1641N, HH34, and HH1/2. In order to understand the connection between the submillimeter clumps and the formation of stars, it is useful to correlate the SCUBA clumps with excited H_2 2.122 μm emission which traces the energetic shocks known to emerge from young protostars. Fortunately, Stanke (2000) and Stanke, McCaughrean, and Zinnecker (2002; SMZ) mapped most of the Orion A cloud in this transition, providing an excellent resource for this analysis.

4.1. Correlation of Clumps with H_2 Shock Emission

The presence of shock excited H_2 emission near individual clumps provides an attractive sign post for an embedded protostellar source. Walawender et al. (2005, 2006) have shown that the combination of 2.122 μm H_2 shock observations and 850 μm continuum emission maps can help identify which submillimeter clumps are associated with Class 0 sources. Walawender et al. find that the presence of H_2 emission correlates reasonably well with the concentration of the submillimeter clumps, such that more concentrated sources have a higher likelihood of harboring embedded protostars. This is to be expected from the simple theoretical identification of the clumps with Bonnor-Ebert spheres, where higher concentration corresponds to the clump being closer to gravitational instability.

The investigations by Walawender et al. (2005, 2006) of regions within Perseus provide statistics on only a handful of submillimeter clumps. The present analysis of Orion A South allows for a much more robust investigation. Seventy of the seventy-one clumps obtained from the submillimeter map lie within the boundary of the H₂ 2.122 μm region mapped by Stanke (2000) and seventeen of these clumps have clearly associated H₂ emission (see Table 3 and Figures 9 through 17). A comparison between the presence of H₂ and the observational (physical) properties of the submillimeter clumps strengthens the results of Walawender et al. Tables 4-6 tabulate the correlation between the presence of molecular hydrogen versus total flux (mass), peak flux (column density), and concentration (importance of self-gravity). There exists no discernible correlation between the presence of H₂ emission and total flux, suggesting that clump mass is not a significant determinant for collapse of a starless core. There are, however, strong correlations with peak flux and concentration, suggesting that column density and the balance between self-gravity and thermal stability are significant in determining collapse.

4.2. Details on Individual Regions with Orion A South

4.2.1. OMC4

The southern portion of the ISF contains a cluster of about two dozen SCUBA sources embedded in a pair of V-shaped north-south ridges, denoted OMC4 by Johnstone & Bally (1999). The northern end of this cluster of clumps appears to be interacting with the southern portion of the Orion Nebula. An extensive network of fluorescent H₂ filaments wrap around the northern boundary of these clumps. Additionally, high resolution Hubble Space Telescope (HST) H α images reveal many young stars, proplyds, and Herbig-Haro objects in this region (Bally et al. 2006). There is not a simple correspondence between individual YSOs and SCUBA clumps, suggesting that little circumstellar material remains for the optically visible sources. It is likely that the expanding Orion Nebula has recently overrun this region, uncovering many young stars. Interestingly, few SCUBA clumps are coincident with IRAS point sources, 2 μm sources, or H₂ outflows. Thus, most of these clumps do not contain obvious protostars or YSOs. Stanke (2000) does report several H₂ flows in the region (Stanke 2-8, 2-9, 3-1, 3-4, 3-5, 3-8, and 3-10). These may originate in more mature YSOs which have shed their dusty submillimeter envelopes. Figure 9 shows the OMC4 region.

A large, arcminute-scale H₂ flow consisting of Stanke 2-7 and 3-2 (SMZ29) emerges from a dim SCUBA clump located at J(2000) = 5:34:40.9, -5:31:47 about 8' west of the OMC4 region at PA \sim 340°. The clump is clearly real, but located too close to the edge of the

mapped SCUBA field for inclusion in our clump catalog. A bright K-band reflection nebula opens towards the north-northwest.

Stanke 3-11 is a northeast facing bow shock emerging from SMM 053474-05414 (ID 01) at PA $\sim 40^\circ$. IRAS 05322-0543 may be associated with this clump and outflow.

The K-band star at J(2000) = 5:34:35.7, -5:40:10 embedded in a dim, uncatalogued SCUBA clump located at the western edge of our mapped region may be the driving source of the chain of H₂ shocks Stanke 3-6, 3-7, and 3-9 (SMZ31) which extends to the northwest at PA $\sim 335^\circ$ with respect to this clump.

Finally, a fan-shaped reflection nebula opens towards the northeast from another uncatalogued SCUBA clump at J(2000) = 5:34:48.9, -5:41:42 at the southern end of OMC4. No shocks are detected along its axis.

4.2.2. OMC5 behind NGC 1980

The region situated at the southern end of the ISF about 30' south of the Orion Nebula contains a loose cluster of SCUBA clumps located immediately behind the star cluster NGC 1980. We denote the region as OMC5. The cluster of submillimeter clumps contains at least one IRAS source (IRAS 05328-6000), but this is a lower limit to embedded YSOs as confusion within this region limits the usefulness of the IRAS data.

The faint H₂ jet, Stanke 3-17 (SMZ37), emerges parallel to a reflection nebula at PA $\sim 35^\circ$. This feature emerges from the southern edge of a faint SCUBA clump (not listed in Table 1) at J(2000) = 5:35:04.5, -5:51:50. Stanke 3-16 north of this feature appears to emerge from SMM 053514-05513 (ID 25) at PA $\sim 320^\circ$. Figure 10 shows the H₂ emission and 850 μm contours in this region.

A chain of H₂ shocks was detected by Stanke (2000) which consists of Stanke 4-1, 4-2, and 4-3 (Position Angle, PA $\sim 335^\circ$) emerging from a faint, fan-shaped reflection nebula oriented towards the north-northwest. These features appear to emanate from SCUBA clump SMM 053515-05558 (ID 30) which exhibits a faint, K-band reflection nebula opening towards the north-northwest (see Figure 11). The morphology of these latter shocks consist of north-facing bows consistent with an outflow emerging from the clump. Stanke 4-5 may trace a counterflow on the other side of this clump, or possibly a flow from an adjacent clump. This sub-millimeter clump apparently contains a Class 0 YSO driving a bipolar outflow visible in H₂ (SMZ38). No optical HH objects are detected in the vicinity of this flow, therefore it must be embedded.

The H₂ features Stanke 4-4, 4-5, 4-6 and 4-7 cluster around SMM 053520-05571 (ID 37) and may trace outflows emerging from this clump., including SMZ39. SCUBA clump SMM 053515-05584 (ID 31) south of SMZ38 is at the center of the flow SMZ39 and therefore may contain the driving source.

Several isolated SCUBA clumps are located south of NGC 1980. Three infrared point sources are embedded within this region. IRAS 05331-0606 is located at the north-end of a ridge containing the diffuse dust clumps SMM 053568-06057 (ID 44), 053571-06077 (ID 45), and 053573-06078 (ID 46). A bright H₂ shock and HH object located at J(2000) = 5:35:37.3, -6:02:32 several arcminutes north-northeast of IRAS 05331-0606 has a bow shape consistent with a flow emerging from the vicinity of this IRAS source (Stanke 4-9; SMZ40 - not shown).

IRAS 05334-0611 is associated with a star embedded within SMM 053586-06100 (ID 47). This star appears to drive a pair of H₂ bubbles designated Stanke 5-2 (SMZ43) towards PA $\sim 70/250^\circ$ (Figure 12).

IRAS 05329-0614 is coincident with SMM 053537-06131 (ID 40) and appears to drive a long 17' long H₂ and HH flow towards PA $\sim 70/250^\circ$ (see Figure 12). A conical reflection nebula opening towards the southwest is evident in the K-band images of Stanke (2000) and a 10 to 20'' long H₂ jet (Stanke 4-12) emerges along this axis. A large (3' diameter), faint, complex of HH objects seen as faint [S II] and H α filaments are located 14' southwest of this source between J(2000) = 5:34:22.8, -6:18:19 and 5:34:24.22 -6:15:13. A bright but compact HH object is found 3' to the northeast at J(2000) = 5:35:34.75 -6:12:04. The curvatures of the various filaments in these HH objects are consistent with being driven by a jet or outflow from IRAS 05329-0614. The H₂ portions of this flow are designated Stanke 4-11 and 4-12 (SMZ42).

SCUBA clump SMM 053660-06149 (ID 65), located due north of the L1641N cluster, contains a K-band source and a wide-angle H₂ flow (Stanke 5-5; SMZ46) that appears to propagate towards PA $\sim 20/200^\circ$. The clump is located at the southeast end of a filament of molecular gas and chain of clumps (SMM 053618-06106 (ID 48), 053637-06129 (ID 55), 053641-06140 (ID 57), and 053645-06145 (ID 61)) which contain no IRAS sources or H₂ objects.

4.2.3. L1641N

This region contains a dense cluster of about 100 embedded stars, including moderate-luminosity IR sources, including IRAS 05338-0624 and IRAS 05339-0626 (Figure 13). Dozens of HH and H₂ flows (Stanke Field 5) appear to be bursting out of this cluster in all directions

(Stanke 2000; Reipurth, Bally, and Devine 1997). At least two flows have reached parsec-scale dimensions, and their northern lobes have propagated large bow shocks currently impinging on the outskirts of the Orion Nebula about a degree to the north. About a dozen SCUBA clumps are associated with the L1641 cluster. The region is too confused to make specific associations between individual outflows, clumps, and stars (see Figure 13). The outflows SMZ48, 49, 50, 51, 53, and 54 emerge from this cluster. Reipurth et al. (1997) proposed that several giant HH flows extend for beyond the molecular cloud for over 10 pc from this cluster. One of these flows may be related to the north-south H₂ flow SMZ 49. It has also been suggested that the giant HH bow shock HH131 located 2.5 degrees south originates here (Wang et al. 2005).

SCUBA clump SMM 053641-06226 (ID 58) is located on the east side of the L1641N cluster and appears to be associated with a large H₂ and Herbig-Haro flow SMZ51 that emerges from the L1641N region towards PA $\sim 80^\circ$ and that is associated with HH 301 and possibly HH 302.

The flow SMZ54 emerges from a prominent disk shadow in both visual and near-IR images located midway between two SCUBA clumps (ID 54 and 58). Although we did not resolve a clump associated with this edge-on disk, there is bright extended 850 μm emission in this region.

SCUBA clump SMM053631-06221 (ID 52) is embedded in the center of the L1641N cluster and may be associated with IRAS 05338-0624. This object is located at the base of the giant SMZ 49 outflow which is associated with HH 306 – 310. The orientation and shapes of associated bow shocks indicate that this flow is propagating at PA $\sim 355^\circ$ through a giant cavity on the east side of the Integral Shaped Filament. The terminal shocks of this flow at its north end may be interacting with the southern boundary of the Orion Nebula (Reipurth et al. 1998).

4.2.4. HH 34

The SCUBA clump 053550-06269 (ID 41) is associated with the spectacular HH 34 jet and the chain of HH objects which delineate its parsec-scale outflow (Devine et al. 1997; SMZ55 - indicated by a dashed line in Figures 14 and 15). Another clump, 053551-06265 (ID 42), appears associated with HH 34 IRS5, an embedded near-IR star responsible for a bright south-facing reflection nebula located on the eastern edge of the HH 34 cloud core. The H₂ flow Stanke 5-24 (SMZ56) appears to trace an embedded jet from yet another star in this region, although no connection with a SCUBA clump is observed. Thus, the cloud

core surrounding the HH 34 source appears to have spawned a small group of YSOs.

A diffuse group of faint SCUBA clumps lies half-way between HH 34 and L1641N several arcminutes southeast of the enigmatic object HH 222 whose filaments resemble a waterfall (Castets et al. 2004). At least one K-band star in the complex of faint dust emission illuminates a fan-shaped reflection nebula opening towards the southwest. It is possible that HH 222 wraps around the northwest rim of this cluster of dust clouds.

4.2.5. *South of L1641N*

Several SCUBA sources south of L1641N but north of HH 1/2 drive interesting outflows. SCUBA clump SMM 053660-06389 (ID 66 - Figure 16) is not associated with an IRAS point source but drives a stunning bipolar H₂ flow at PA $\sim 170/350^\circ$ (Stanke 5-28 = SMZ59). The embedded source YSO is likely to be an isolated Class 0. The SCUBA clump is elongated along the outflow axis. This source was mapped in CO by Levreault (1988) and Morgan et al. (1991) who designated it as V380 Ori NE. Detailed H₂, interferometric CO, and SCUBA observations were presented by Davis et al. (2000).

SCUBA source SMM 053700-06272 (ID 70 - Figure 16), located several arcminutes northeast of SMM 053660-06389, is associated with a northeast facing reflection nebula and drives an H₂ flow, Stanke 5-27 (SMZ58). A faint [S II] dominated HH knot is associated with the northeast end of this flow. The embedded YSO is likely to be a Class O source since there is no IRAS source coincident with this clump. The SCUBA clump is elongated orthogonal to the outflow axis.

The several IRAS sources in this region are not associated with SCUBA clumps. For example, IRAS 05342-0635 seems to be associated with a visible and near-IR star which exhibits no outflow activity in either H₂ or visual wavelength images. The dust from this star may trace a remnant disk or envelope which has not fueled accretion onto the star in recent times. In contrast, IRAS 05345-0635 is associated with the $m_R = 12$ magnitude star to BE Ori which drives a spectacular HH jet at PA $\sim 45^\circ$ (SMZ57). Interestingly, this star is not associated with a SCUBA source. Perhaps it lacks an extended, cool, and inactive outer envelope but still retains an inner disk which is actively fueling accretion and outflow.

4.2.6. *NGC 1999 and HH 1/2*

A cluster of 4 SCUBA clumps, 053629-06474 (ID 50) , 053631-06455 (ID 53), 053638-06461 (ID 56), and 053642-06249 (ID 60), are located south of the visually-bright NGC 1999

reflection nebula powered by V380 Ori and are associated with YSOs in the vicinity of the Herbig-Haro objects HH 1/2 (see Figure 17). Interestingly, NGC 1999/V380 Ori, at the northern end of this sub-cluster, is not coincident with a SCUBA source. Thus, this star must be relatively clear of circumstellar dust.

Clump SMM 053638-06461 (ID 56), centered on the source of the HH 1/2 bipolar outflow, is the brightest 850 μm source in this complex (see Figure 17). IRAS did not detect a point source here; nevertheless, the YSO embedded in this clump drives one of the brightest and most spectacular HH flows in the sky, the objects HH 1 and 2 (Stanke 6-10 and 6-15; SMZ64).

The second brightest clump, SMM 053631-06455 (ID 53), located near the H₂O maser source northwest of HH 1/2 is associated with IRAS 05338-0647. Stanke 6-11 is located near this source. From the morphology of the H₂ emission, it is likely that this feature and Stanke 6-6 (which coincides with HH 3) are driven by this source.

Clump SMM 053641-06447 (ID 59), located between the HH 1/2 source region and NGC 1999 is associated with IRAS 05339-0646, a visible star ($m_R \sim 16$ mag L1641-KMS31), several faint HH objects (HH 147), and the H₂ features Stanke 6-12 (SMZ63).

Clump 053629-06474 (ID 50), located several arcminutes southwest of HH 1/2 source, is the brightest part of several filaments of dust emission which point radially away from clump 053642-06249, located northeast of the the HH 1/2 core. No IRAS source, star or outflow is associated with this feature. These radial filaments are reminiscent of the network of dust filaments which point away from luminous centers of star formation in the OMC1 cloud core in the middle of the ISF, and from the NGC 1333 star forming complex in the Perseus molecular cloud. The filaments may be the walls of ancient outflow cavities. Alternatively they may be cometary cloud-tails located in the shadows of dense clumps illuminated by UV or shock-heated by winds.

5. Conclusions

Using the techniques developed in Papers I-IV we have identified 71 submillimeter clumps within a 2300 arcmin² region of Orion A South. We have been able to derive estimated masses and temperatures for the majority of the clumps by noting that they can be modeled as Bonnor-Ebert spheres; that is, they can be approximated by almost constant density models with low internal velocities. On this basis the typical clump temperature is found to be 22 ± 5 K; this value is in reasonable agreement with that (18 ± 9 K) derived from the spectral indices obtained from the 850 and 450 μm data. Thus for most of the clumps

a temperature of 20 K is a good working approximation, similar to the results in Orion B (Papers III and IV).

The mass function of submillimeter clumps found in Orion A South is steeper than the molecular cloud mass spectrum, suggesting that most of the mass of submillimeter clumps lies in small mass objects. This is in agreement with the results in other nearby regions (Motte et al. 1998; Paper II; Paper III; Motte et al. 2001; Paper IV) although the mass function found here is somewhat steeper still than the mass functions derived for these other regions.

A comparison of the appearance of molecular hydrogen shock excited emission and the location of submillimeter clumps reveals that concentration and central column density of the clumps are correlated with evidence of internal protostellar activity. Several new Class O sources have been identified in Orion A South using this technique.

The research of D.J. is supported through a grant from the Natural Sciences and Engineering Research Council of Canada. The JCMT is operated by the Joint Astronomy Centre on behalf of the Particle Physics and Astronomy Research Council of the UK, the Netherlands Organization for Scientific Research, and the National Research Council of Canada. The authors acknowledge the data analysis facilities provided by the Starlink Project which is run by CCLRC on behalf of PPARC. We thank the anonymous referee for suggestions which significantly improved this paper. We thank Thomas Stanke for providing us with his $2.122\mu\text{m}$ images in electronic form. We also thank Rachel Friesen and Helen Kirk for critical reading of this manuscript. J.B. acknowledges support from NASA grants NAG5-8108 (LTSA), the University of Colorado Center for Astrobiology and NASA grant NCC2-1052, and National Science Foundation grants AST 0407356 and AST 9819820.

REFERENCES

- Ali, B., & Noriega-Crespo, A. 2004, *ApJ*, 613, 374
- Bally, J., Licht, D., Smith, N., & Walawender, J. 2006, *AJ*, 131, 473
- Beuther, H., Schilke, P., & Wyrowski, F. 2004, *ApJ*, 616, 23
- Bonnor, W.B. 1956, *MNRAS*, 116, 351
- Brown, A.G.A., de Geus, E.J., & de Zeeuw, P.T. 1994, *A&A*, 289, 101
- Castets, A., Reipurth, B., & Loinard, L. 2004, *A&A*, 427, 895
- Chen, H. & Tokunaga, A.T. 1994, *ApJS*, 90, 149
- Davis, C. J., Dent, W. R. F., Matthews, H. E., Coulson, I. M., & McCaughrean, M. J. 2000, *MNRAS*, 318, 952
- Devine, D., Bally, J., Reipurth, B., & Heathcote, S. 1997, *AJ*, 114, 2095
- Ebert, R. 1955, *Zs.Ap.*, 37, 217
- Friesen, R.K., Johnstone, D., Naylor, D.A., & Davis, G.R. 2005, *MNRAS*, 361, 460
- Goldsmith, P.F., Bergin, E.A., & Lis, D.C. 1997, *ApJ*, 491, 615
- Hartmann, L. 1998, *Accretion Processes in Star Formation* (Cambridge: University Press)
- Henning, Th., Michel, B., & Stognienko, R. 1995, *Planetary Space Science*, (special issue: Dust, molecules, and backgrounds), 43, 1333
- Hogerheijde, M.R. & Sandell, G. 2000, *ApJ*, 534, 880
- Holland, W.S. et al. 1999, *MNRAS*, 303, 659
- Hoogerwerf, R., de Bruijne, J.H.J., & de Zeeuw, P.T. 2001, *A&A*, 365, 49
- Jenness, T., Stevens, J.A., Archibald, E.N., Economou, F., Jessop, N.E., & Robson, E.I. 2002, *MNRAS*, 336, 14
- Johnstone, D. & Bally, J. 1999, *ApJ*, 510, L49
- Johnstone, D., Boonman, A.M.S., & van Dishoeck, E.F. 2003, *A&A*, 412, 157
- Johnstone, D., Di Francesco, J, Kirk, H 2004, *ApJ*, 611, L45
- Johnstone, D., Wilson, C.D., Moriarty-Schieven, G., Creighton, J.G., & Gregersen, E. 2000a (Paper I), *ApJS*, 131, 505
- Johnstone, D., Wilson, C.D., Moriarty-Schieven, G., Joncas, G., Smith, G., Gregersen, E., & Fich, M. 2000b (Paper II), *ApJ*, 545, 327
- Johnstone, D., Fich, M., Mitchell, G.F., & Moriarty-Schieven, G. (Paper III), *ApJ*, 559, 307

- Johnstone, D., Matthews, H., & Mitchell, G.F. 2006 (Paper IV), *ApJ*, 639, 259
- Jorgensen, J.K., Johnstone, D., Kirk, H., & Myers, P.C. 2006, *ApJ*, submitted
- Kerton, C.R., Martin, P.G., Johnstone, D., & Ballantyne, D.R. 2001, *ApJ*, 552, 601
- Kirk, H., Johnstone, D., & Di Francesco, J. 2006, *ApJ*, 646, 1009
- Kramer, C., Stutzki, J., Röhrig, R., & Corneliusen, U. 1998, *A&A*, 329, 249
- Kroupa, P., Tout, C. & Gilmore, G. 1993, *MNRAS*, 262, 545
- Kroupa, P. 2002, *Science*, 295, 82
- Levreault, R. 1988, *ApJS*, 67, 283
- McKee, C.F. & Williams, J.P. 1997, *ApJ*, 476, 144
- Mookerjea, B., Kramer, C., Nielbock, M., & Nyman, L.-A. 2004, *A&A*, 426, 119
- Morgan, J.A., Schloerb, F.P., Snell, R.L., & Bally, J. 1991, *ApJ*, 376, 618
- Motte, F., André, P., & Neri, R. 1998, *A&A*, 336, 150
- Motte, F., André, P., Ward-thompson, D., & Bontemps, S. 2001, *A&A*, 372L, 41
- Onishi, T., Mizuno, A., Kawamura, A., Tachihara, K., & Fukui, Y. 2002, *ApJ*, 575, 950
- Ogura, K. 1995, *ApJ*, 450, L23
- Reid, M.A. & Wilson, C.D. 2005, *ApJ*, 629, 891
- Reipurth, B., Bally, J. & Devine, D. 1997, *AJ*, 114, 2708
- Reipurth, B., Devine, D., & Bally, J. 1998, *AJ*, 116, 1396
- Scalo, J. 1986, *Fundamentals of Cosmic Physics*, 11, 1
- Stanke, T., PhD Thesis, University of Potsdam
- Stanke, T., McCaughrean, M. J., & Zinnecker, H. 2002, *A&A*, 392, 239
- Stutzki, J. & Güsten, R. 1990, *ApJ*, 356, 513
- Testi, L. & Sargent, A.I. 1998, *ApJ*, 508, L91
- van der Tak, F.F.S., van Dishoeck, E.F., Evans, N.J. II, & Bakker, E.J. 1999, *ApJ*, 522, 991
- Visser, A.E., Richer, J.S., Chandler, C.J., & Padman, R. 1998, *MNRAS*, 301, 585
- Wang, M., Noumaru, J., Wang, H., Yang, J., Chen, J. 2005, *AJ*, 130, 2745
- Walawender, J., Bally, J., Kirk, H., & Johnstone, D. 2005, *AJ*, 130, 1795
- Walawender, J., Bally, J., Kirk, H., Johnstone, D., Reipurth, B., & Aspin, C. 2006, *AJ*, 132,

Williams, J.P., Blitz, L, & McKee, C.F. 2000, in Protostars and Planets IV, ed. V. Mannings, A. P. Boss & S. S. Russell (Tucson: University of Arizona Press), 97

Williams, J.P., de Geus, E.,J., & Blitz L. 1994, ApJ, 428, 693

Williams, J.P. & McKee, C.F. 1997, ApJ, 476, 166

Table 1. Clump properties in Orion A South derived from 850 μ m data.

Name ^a (SMM J)	ID	R.A. ^b (J2000)	Dec. ^b (J2000)	S_{850} ^c (Jy)	S_{850}^{peakc} (Jy/bm)	R_{eff}^c (10^3 AU)	C^d	T_d^d (K)	$\log P/k^d$ (K/cm ³)	$M_{T_d}^d$ (M_{\odot})	$M_{T_d=20\text{K}}^e$ (M_{\odot})
053474-05414	01	05:34:44.2	-05:41:27	0.78	0.41	7	0.47	14	6.3	1.11	0.63
053484-05462	02	05:34:50.6	-05:46:15	2.81	0.35	13	0.39	25	6.0	1.64	2.26
053486-05389	03	05:34:51.4	-05:38:54	0.76	0.29	7	0.36	24	6.2	0.47	0.61
053487-05423	04	05:34:52.0	-05:42:18	1.73	0.24	12	0.33	29	5.9	0.83	1.39
053490-05463	05	05:34:54.0	-05:46:18	4.23	0.75	13	0.53	20	6.2	3.40	3.40
053492-05435	06	05:34:55.2	-05:43:30	7.12	0.42	20	0.39	31	5.9	3.12	5.72
053494-05460	07	05:34:56.2	-05:46:03	7.76	1.20	17	0.69	20	5.9	6.23	6.23
053495-05415	08	05:34:57.0	-05:41:33	6.46	0.44	19	0.42	27	5.9	3.40	5.19
053496-05435	09	05:34:57.6	-05:43:33	2.24	0.29	13	0.39	23	5.9	1.47	1.80
053497-05365	10	05:34:58.2	-05:36:30	2.17	0.31	12	0.34	32	6.0	0.91	1.74
053497-05409	11	05:34:58.2	-05:40:54	4.43	0.37	17	0.46	21	5.9	3.31	3.56
053499-05441	12	05:34:59.4	-05:44:09	1.96	0.24	13	0.33	30	5.9	0.90	1.58
053500-05389	13	05:35:00.2	-05:38:57	6.87	0.61	17	0.49	23	6.0	4.51	5.53
053501-05400	14	05:35:00.4	-05:40:03	2.70	0.42	13	0.48	18	6.0	2.55	2.17
053503-05556	15	05:35:01.8	-05:55:36	3.64	0.53	14	0.53	18	6.0	3.43	2.92
053504-05372	16	05:35:02.6	-05:37:12	4.12	0.61	12	0.39	30	6.2	1.89	3.31
053504-05379	17	05:35:02.4	-05:37:54	6.79	0.76	15	0.49	24	6.1	4.20	5.45
053505-05362	18	05:35:03.0	-05:36:12	11.03	0.98	19	0.55	24	6.0	6.82	8.87
053508-05374	19	05:35:05.0	-05:37:24	6.68	1.02	13	0.49	25	6.3	3.91	5.37
053509-05348	20	05:35:05.2	-05:34:48	9.60	0.96	17	0.54	24	6.1	5.94	7.72
053510-05331	21	05:35:06.0	-05:33:09	3.70	0.62	14	0.57	17	6.0	3.81	2.97
053511-05339	22	05:35:06.6	-05:33:57	3.62	0.52	13	0.43	23	6.1	2.38	2.91
053513-05567	23	05:35:07.6	-05:56:42	1.01	0.37	8	0.44	16	6.2	1.15	0.81
053514-05359	24	05:35:08.4	-05:35:57	9.95	1.38	16	0.60	24	6.2	6.15	8.00
053514-05513	25	05:35:08.4	-05:51:21	4.69	0.62	15	0.51	20	6.0	3.77	3.77
053514-05579	26	05:35:08.6	-05:57:57	1.85	0.38	10	0.39	23	6.2	1.22	1.49
053514-06136	27	05:35:08.4	-06:13:39	4.45	0.45	16	0.48	20	5.9	3.58	3.58
053515-05342	28	05:35:08.8	-05:34:15	3.84	0.38	14	0.28	39	6.1	1.26	3.09
053515-05533	29	05:35:08.8	-05:53:18	0.83	0.30	8	0.41	17	6.2	0.86	0.67
053515-05558	30	05:35:09.0	-05:55:51	7.67	1.50	17	0.75	19	5.8	6.66	6.17
053515-05584	31	05:35:09.2	-05:58:27	2.50	0.69	12	0.65	15	6.0	3.16	2.01
053516-05379	32	05:35:09.8	-05:37:54	1.64	0.37	10	0.43	18	6.1	1.54	1.32
053516-05522	33	05:35:09.4	-05:52:12	2.92	0.52	12	0.48	19	6.1	2.53	2.34
053517-05351	34	05:35:10.4	-05:35:06	6.47	0.94	13	0.48	25	6.3	3.78	5.20
053518-06139	35	05:35:10.8	-06:13:57	8.40	0.54	21	0.54	21	5.8	6.28	6.75
053520-05345	36	05:35:12.0	-05:34:30	6.35	0.94	15	0.62	20	6.0	5.10	5.10
053520-05571	37	05:35:12.2	-05:57:06	2.20	0.48	11	0.47	18	6.1	2.07	1.77
053523-05579	38	05:35:13.6	-05:57:57	4.19	0.85	14	0.66	17	5.9	4.31	3.36
053524-05332	39	05:35:14.6	-05:33:15	1.73	0.26	12	0.37	25	6.0	1.01	1.39
053537-06131	40	05:35:22.0	-06:13:06	1.24	0.29	9	0.36	27	6.1	0.65	0.99
053550-06269	41	05:35:29.8	-06:26:57	3.40	0.94	14	0.76	15	5.8	4.30	2.74
053551-06265	42	05:35:30.6	-06:26:30	1.89	0.39	11	0.45	18	6.1	1.78	1.52
053562-06097	43	05:35:37.2	-06:09:42	0.39	0.30	5	0.37	20	6.4	0.32	0.32
053568-06057	44	05:35:41.0	-06:05:45	2.36	0.24	14	0.36	31	5.8	1.04	1.90
053571-06077	45	05:35:42.4	-06:07:45	1.98	0.28	12	0.35	31	6.0	0.87	1.59

Table 1—Continued

Name ^a (SMM J)	ID	R.A. ^b (J2000)	Dec. ^b (J2000)	S_{850} ^c (Jy)	S_{850}^{peak} ^c (Jy/bm)	R_{eff} ^c (10^3 AU)	C ^d	T_d ^d (K)	$\log P/k$ ^d (K/cm ³)	M_{T_d} ^d (M_{\odot})	$M_{T_d=20\text{K}}$ ^e (M_{\odot})
053573-06078	46	05:35:43.6	-06:07:48	2.10	0.28	12	0.34	31	6.0	0.92	1.69
053586-06100	47	05:35:51.8	-06:10:00	1.84	0.57	10	0.60	14	6.0	2.62	1.48
053618-06106	48	05:36:10.8	-06:10:39	5.32	0.87	16	0.68	17	5.8	5.49	4.28
053628-06240	49	05:36:17.0	-06:24:00	1.70	0.30	11	0.39	22	6.0	1.19	1.37
053629-06474	50	05:36:17.6	-06:47:27	1.47	0.24	11	0.35	28	6.0	0.74	1.18
053630-06233	51	05:36:18.2	-06:23:21	3.63	0.40	15	0.44	22	6.0	2.54	2.92
053631-06221	52	05:36:18.6	-06:22:09	27.48	4.69	24	0.86	29	5.9	13.14	22.09
053631-06455	53	05:36:18.4	-06:45:30	8.55	1.31	17	0.69	20	5.9	6.87	6.87
053636-06234	54	05:36:21.6	-06:23:24	5.03	0.46	17	0.46	22	5.9	3.52	4.05
053637-06129	55	05:36:22.0	-06:12:54	3.10	0.30	16	0.43	20	5.8	2.49	2.49
053638-06461	56	05:36:22.6	-06:46:09	12.94	1.99	21	0.79	22	5.8	9.05	10.40
053641-06140	57	05:36:24.6	-06:14:00	5.17	0.57	15	0.48	22	6.0	3.62	4.16
053641-06226	58	05:36:24.6	-06:22:36	10.47	0.88	21	0.64	21	5.8	7.83	8.41
053641-06447	59	05:36:24.8	-06:44:42	5.17	0.65	17	0.60	18	5.9	4.88	4.16
053642-06249	60	05:36:25.0	-06:24:54	14.00	1.24	21	0.64	24	5.9	8.66	11.25
053645-06145	61	05:36:27.2	-06:14:30	3.82	0.28	17	0.35	36	5.8	1.38	3.07
053648-06250	62	05:36:28.8	-06:25:00	2.02	0.28	12	0.31	31	6.0	0.89	1.63
053652-06252	63	05:36:31.2	-06:25:15	1.89	0.33	11	0.41	21	6.1	1.42	1.52
053655-06262	64	05:36:32.8	-06:26:15	3.32	0.34	15	0.43	21	5.9	2.49	2.67
053660-06149	65	05:36:36.2	-06:14:57	1.30	0.38	9	0.50	15	6.1	1.65	1.05
053660-06389	66	05:36:36.0	-06:38:54	6.82	1.09	23	0.84	16	5.4	7.74	5.48
053669-06262	67	05:36:41.4	-06:26:15	12.04	0.90	24	0.67	21	5.7	9.01	9.68
053682-06287	68	05:36:49.0	-06:28:42	4.62	0.36	18	0.48	19	5.8	4.01	3.72
053685-06298	69	05:36:51.2	-06:29:51	1.55	0.25	11	0.35	28	5.9	0.78	1.25
053700-06372	70	05:37:00.0	-06:37:12	3.41	0.61	13	0.58	17	6.0	3.52	2.74
053728-06498	71	05:37:16.8	-06:49:48	1.34	0.49	9	0.53	15	6.2	1.70	1.08

^aName formed from J2000 positions (hhmm.mmddmm.m).

^bPosition of peak surface brightness within clump (accurate to 3'').

^cRadius, peak flux, and total flux are derived from `clfind` (Williams et al. 1994). The peak flux and total flux have uncertainties of about 20%, mostly due to absolute flux calibration. The radius has not been deconvolved from the telescope beam.

^dQuantities derived from Bonnor-Ebert analysis (see text).

^eMass derived from the total flux assuming $T_d = 20$ K and $\kappa_{850} = 0.02$ cm²g⁻¹.

Table 2. Submillimeter wavelength properties of clumps in Orion A South

Name ^a (SMM J)	S_{450}/S_{850} ^b	$S_{450}^{\text{peak}}/S_{850}^{\text{peak}}$ ^b	$T_d(\text{BE})^c$ (K)	$T_d(\text{SM})$ Best ^d (K)	$T_d(\text{SM})$ Range ^d (K)
053474-05414	5.9	6.0	14	13	8– 24
053484-05462	6.4	6.7	25	14	8– 31
053486-05389	6.4	6.9	24	14	8– 31
053487-05423	6.1	6.9	29	13	8– 26
053490-05463	7.1	7.1	20	16	8– 47
053492-05435	6.7	7.1	31	15	8– 35
053494-05460	7.1	6.7	20	16	8– 48
053495-05415	7.6	7.8	27	18	9– ∞
053496-05435	7.3	7.6	23	17	9– ∞
053497-05365	8.0	9.6	32	20	9– ∞
053497-05409	7.2	7.9	21	16	9– ∞
053499-05441	5.7	6.0	30	12	7– 23
053500-05389	8.2	9.3	23	21	9– ∞
053501-05400	7.2	8.1	18	16	9– ∞
053503-05556	4.6	4.9	18	10	7– 16
053504-05372	9.8	10.2	30	33	11– ∞
053504-05379	9.1	9.5	24	26	10– ∞
053505-05362	10.8	11.2	24	∞	12– ∞
053508-05374	9.0	9.6	25	25	10– ∞
053509-05348	10.3	10.7	24	40	11– ∞
053510-05331	8.5	9.6	17	22	10– ∞
053511-05339	8.4	9.7	23	22	10– ∞
053513-05567	3.4	3.5	16	8	6– 11
053514-05359	10.2	10.0	24	38	11– ∞
053514-05513	4.7	5.3	20	10	7– 16
053514-05579	3.7	4.8	23	9	6– 12
053514-06136	6.7	7.7	20	15	8– 37
053515-05342	10.0	11.4	39	35	11– ∞
053515-05533	4.5	4.5	17	10	7– 15
053515-05558	4.2	4.3	19	10	6– 14
053515-05584	4.5	4.6	15	10	7– 15
053516-05379	4.3	5.7	18	10	6– 14
053516-05522	5.2	5.1	19	11	7– 19
053517-05351	9.8	9.3	25	33	11– ∞
053518-06139	6.8	7.5	21	15	8– 38
053520-05345	10.1	10.5	20	37	11– ∞
053520-05571	3.2	3.5	18	8	6– 10
053523-05579	3.3	3.9	17	8	6– 11
053524-05332	10.8	11.7	25	49	12– ∞
053537-06131	4.3	5.0	27	10	6– 14
053550-06269	2.0	3.3	15	6	5– 8
053551-06265	3.3	4.4	18	8	6– 11
053562-06097	5.9	6.0	20	13	8– 25
053568-06057	7.7	9.0	31	18	9– ∞

Table 2—Continued

Name ^a (SMM J)	S_{450}/S_{850} ^b	$S_{450}^{\text{peak}}/S_{850}^{\text{peak}}$ ^b	$T_d(\text{BE})$ ^c (K)	$T_d(\text{SM})$ Best ^d (K)	$T_d(\text{SM})$ Range ^d (K)
053571-06077	8.0	8.4	31	20	9– ∞
053573-06078	7.4	8.0	31	17	9– ∞
053586-06100	9.5	7.8	14	29	10– ∞
053618-06106	5.1	6.6	17	11	7– 18
053628-06240	8.4	9.3	22	21	9– ∞
053629-06474	5.1	5.3	28	11	7– 18
053630-06233	7.8	11.4	22	19	9– ∞
053631-06221	8.4	7.4	29	22	9– ∞
053631-06455	8.2	9.0	20	21	9– ∞
053636-06234	7.7	7.8	22	18	9– ∞
053637-06129	7.8	9.0	20	19	9– ∞
053638-06461	8.4	9.0	22	22	9– ∞
053641-06140	12.0	11.4	22	∞	13– ∞
053641-06226	7.2	8.0	21	16	8– 49
053641-06447	7.1	6.6	18	16	8– 46
053642-06249	9.0	8.4	24	25	10– ∞
053645-06145	11.3	13.5	36	∞	12– ∞
053648-06250	6.6	9.0	31	15	8– 34
053652-06252	6.8	7.0	21	15	8– 38
053655-06262	6.5	6.7	21	14	8– 32
053660-06149	7.3	9.8	15	17	9– ∞
053660-06389	6.8	7.1	16	15	8– 38
053669-06262	8.3	8.1	21	21	9– ∞
053682-06287	8.7	9.7	19	23	10– ∞
053685-06298	9.6	8.8	28	30	11– ∞
053700-06372	6.6	5.8	17	15	8– 34
053728-06498	6.0	6.7	15	13	8– 26

^aName formed from J2000 positions (hhmm.mmddmm.m).

^bThe 850 μm and 450 μm peak flux and total flux are derived from *clfind* (Williams et al. 1994) after convolution to an identical beam size. The uncertainty in the flux ratios is approximately 50%.

^cQuantity derived from Bonnor-Ebert analysis (see text).

^dQuantity derived from spectral energy fit to 450 and 850 μm integrated fluxes (see text). The range of acceptable temperatures is determined assuming a 50% uncertainty in the flux ratio measurement.

Table 3. H₂ properties of clumps in Orion A South

Name ^a	ID	H ₂ Emission ^b
053474-05414	01	OMC4, Jet-like, PA 40°, Stanke 3-11
053514-05513	25	OMC5, Jet-like, PA 320°, Stanke 3-16
053515-05558	30	OMC5, Jet-like, PA 335°, Stanke 4-1,4-2,4-3
053515-05584	31	OMC5, Diffuse
053520-05571	37	OMC5, Jet-like, Stanke 4-4,4-5,4-6,4-7
053537-06131	40	OMC5, Jet-like, PA 70/250°, Stasnke 4-11, 4-12, IRAS 05329-0614
053550-06269	41	HH34, Jet-like
053551-06265	42	HH34 IRS5, Jet-like
053586-06100	47	OMC5, Bubble, PA 70/250°, Stannke 5-2, IRAS 05334-0611
053631-06221	52	L1641N, Jet-like, PA 355°, HH306–310, IRAS 05338-0624
053631-06455	53	HH1/2, H ₂ O maser source, Jet-like, Stanke 6-6, 6-11, IRAS 05338-0647
053638-06461	56	HH1/2, Jet-like, Stanke 6-10, 6-15
053641-06226	58	L1641N, Jet-like, PA 80°, HH 301
053641-06447	59	HH1/2, Jet-like, Stanke 6-12, IRAS 05339-0646
053660-06149	65	OMC5, Jet-like, PA 20/200°, Stanke 5-5
053660-06389	66	South L1641N, Jet-like, PA 170/350°, Stanke 5-28
053700-06372	70	South L1641N, Jet-like, Stanke 5-27

^aName formed from J2000 positions (hhmm.mmddmm.m).

^bRegion, H₂ appearance, Stanke (2000) shock label, possible IRAS source

Table 4: Correlation between Total Flux and Presence of H₂ Emission

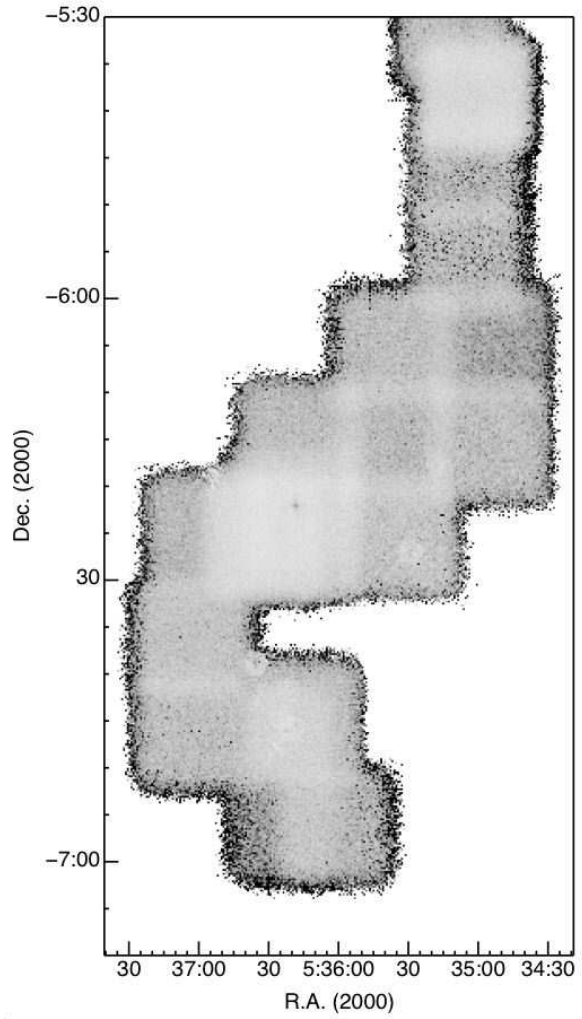
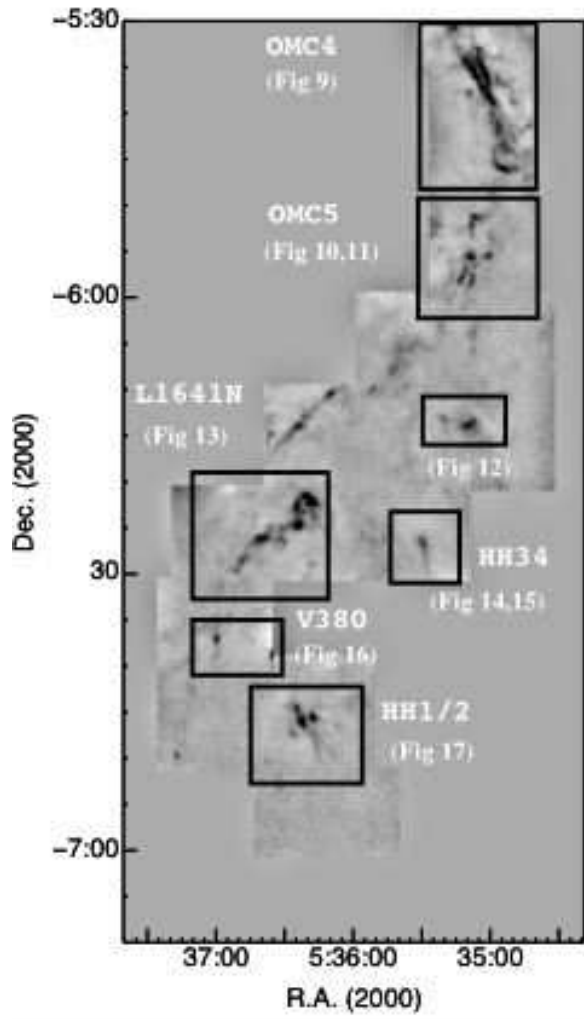
S_{850} (Jy)	Total Clumps	Clumps with H ₂	Percentage
0–10	70	17	24
> 8	10	4	40
6–8	10	2	20
4–6	12	2	17
2–4	20	4	20
< 2	19	5	25

Table 5: Correlation between Peak Flux and Presence of H₂ Emission

S_{850}^{peak} (Jy/bm)	Total Clumps	Clumps with H ₂	Percentage
0–5	70	17	24
> 1.5	3	3	100
1.0–1.5	6	2	33
0.5–1.0	25	6	28
< 0.5	37	5	15

Table 6: Correlation between Concentration and Presence of H₂ Emission

C	Total Clumps	Clumps with H ₂	Percentage
0–1	70	17	24
> 0.7	5	5	100
0.6–0.7	12	5	42
0.5–0.6	10	3	30
0.4–0.5	23	3	13
< 0.4	21	1	5



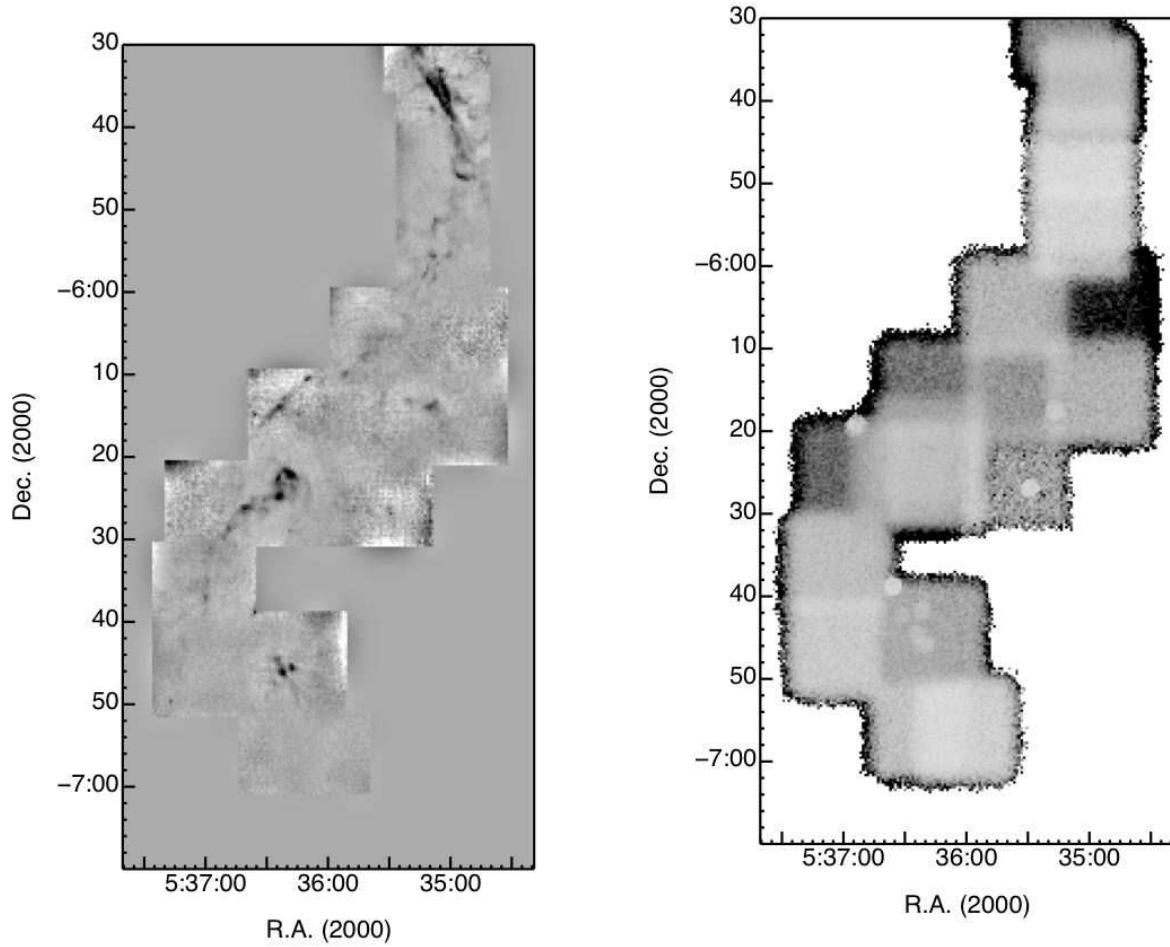


Fig. 1.— (a) The Orion A South region at 850 μm . The star forming regions discussed in the text are labeled. Left: 850 μm emission (greyscale: white to black represents -0.25 to 0.5 Jy bm^{-1}). Right: 850 μm noise map (greyscale: white to black represents 0 to 0.15 Jy bm^{-1}). Note that the noise is systematically lower in regions where multiple observations were taken. (b) The Orion A South region at 450 μm . Left: 450 μm emission (greyscale: white to black represents -1 to 2 Jy bm^{-1}). Right: 450 μm noise map (greyscale: white to black represents 0 to 1 Jy bm^{-1}).

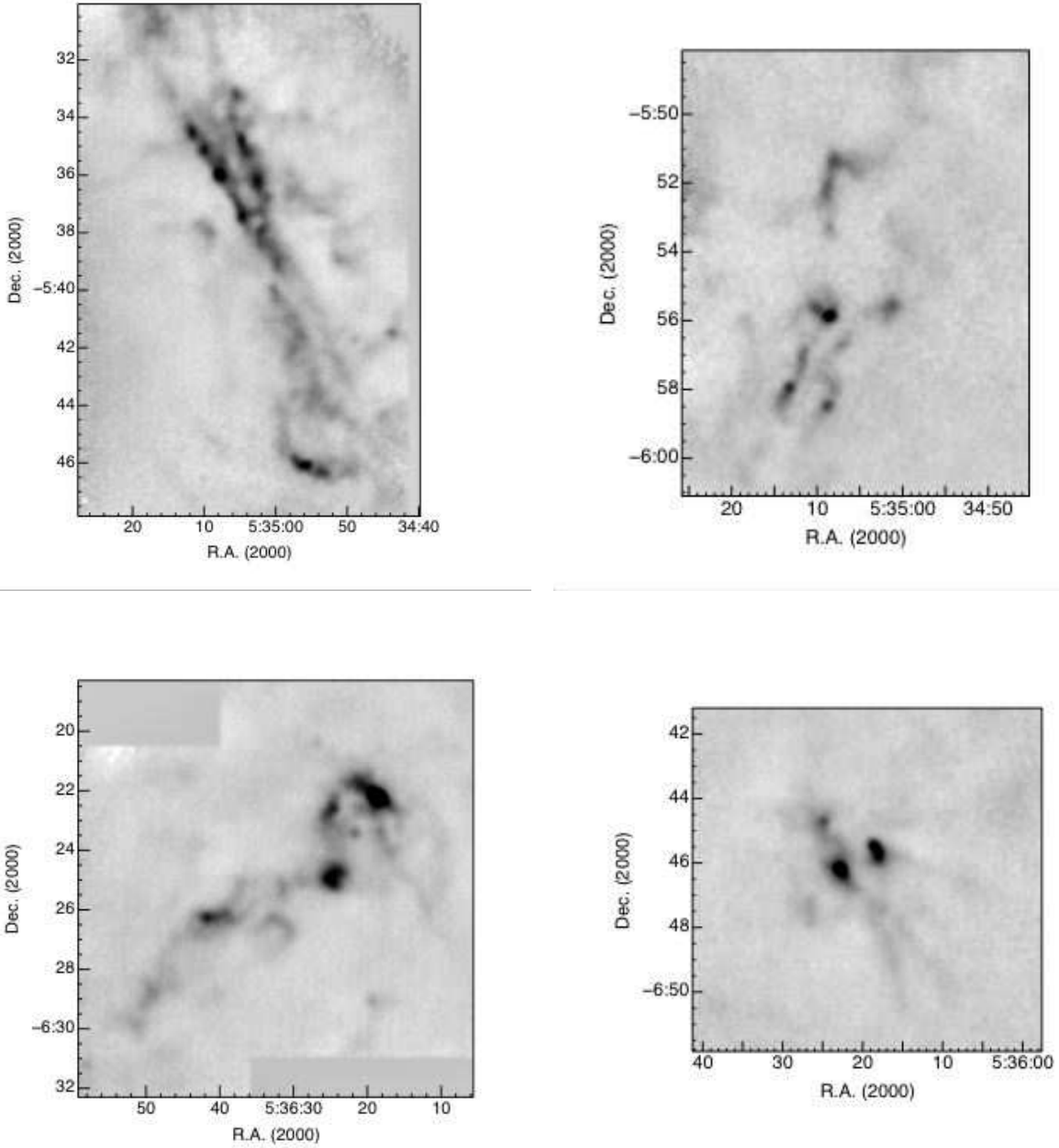


Fig. 2.— Detailed maps of the regions OMC4 (Top Left), OMC5 (Top Right), L1641N (Bottom Left), and HH1/2 (Bottom Right). In all cases the greyscale is white to black, -0.25 to 1.0 Jy bm^{-1} .

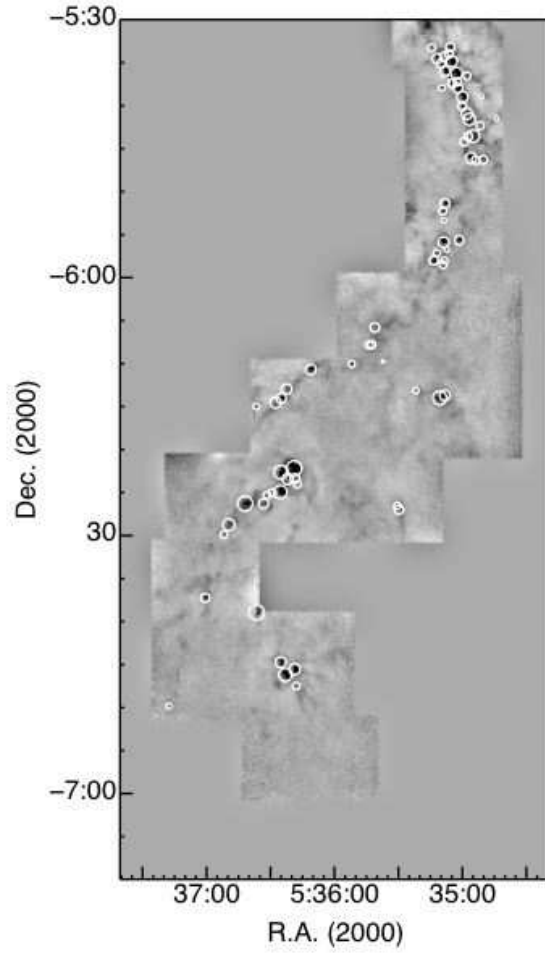


Fig. 3.— Location of the submillimeter clumps found in Orion A South $850\ \mu\text{m}$ using an automated procedure (see text). The circle size represents the area associated with each clump.

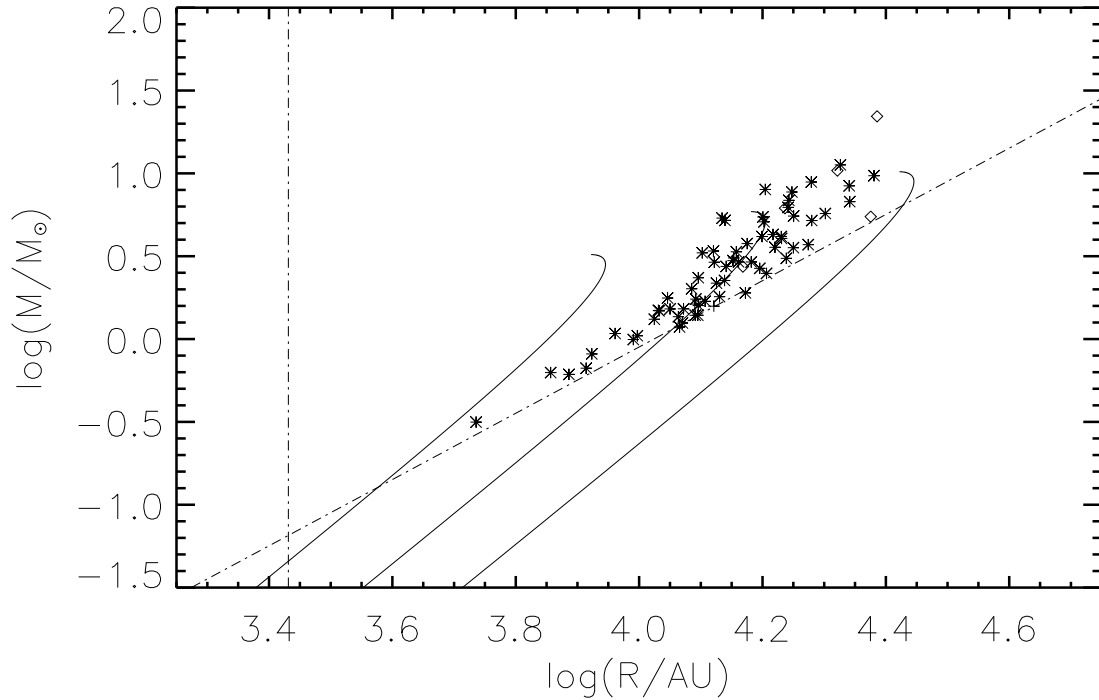


Fig. 4.— Derived mass for each of the 71 clumps vs. the effective radius. Also plotted are the minimum size which a clump might have (resolution limit) and the minimum mass that a clump must have for a given radius such that the clump finding routine can recognize it (approximately 4σ above the background). The symbols denoting each clump are discussed in Figure 5. The three curves from left to right denote the mass-radius relation for Bonnor-Ebert spheres with 20 K internal temperatures, an additional equal internal pressure component due to turbulence, and external pressures $P/k = 0.3, 1.0, 3.3 \times 10^6 \text{ K cm}^{-3}$ (see text).

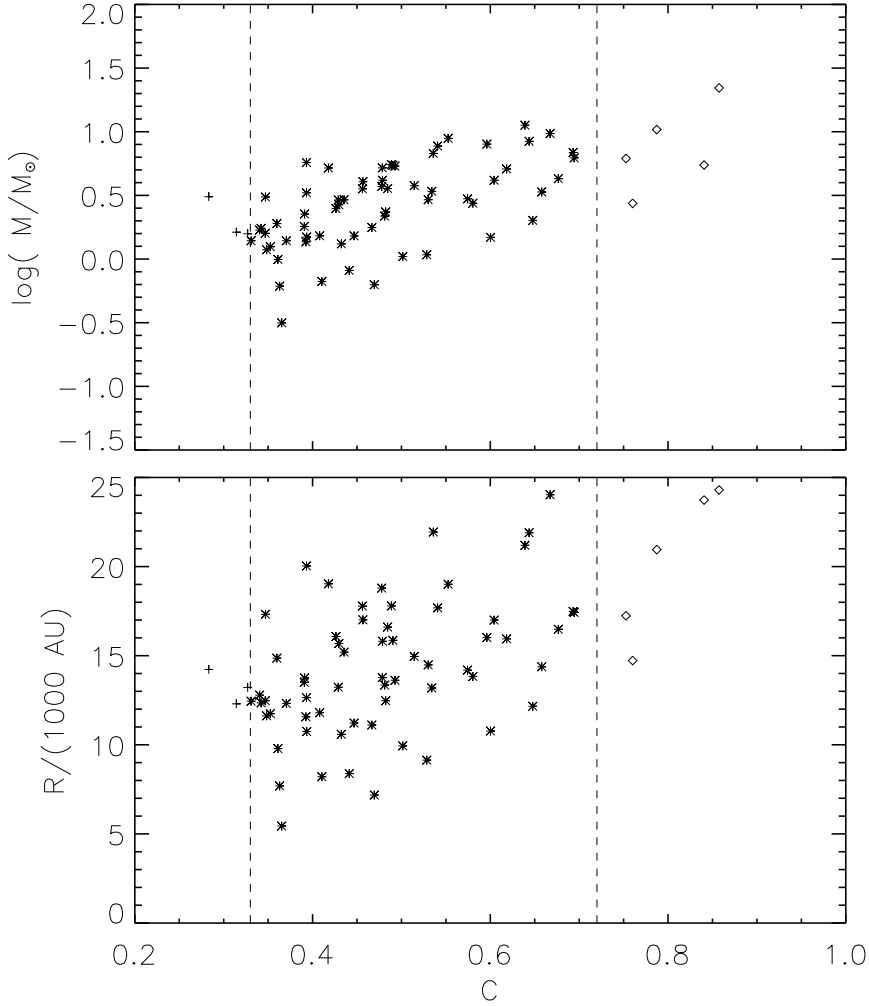


Fig. 5.— Derived concentration for each of the 71 clumps in the Orion A South region (see text). The minimum concentration for a constant density low-mass Bonnor-Ebert sphere is $C = 0.33$, while the maximum concentration beyond which collapse occurs is $C = 0.72$. Clumps with $C > 0.72$ are denoted by diamonds. (Top) Derived mass of the clump vs. concentration. Note that the uncertainty in the mass is about 20%, similar to the spread in the data points. (Bottom) Derived radius of the clump vs. concentration.

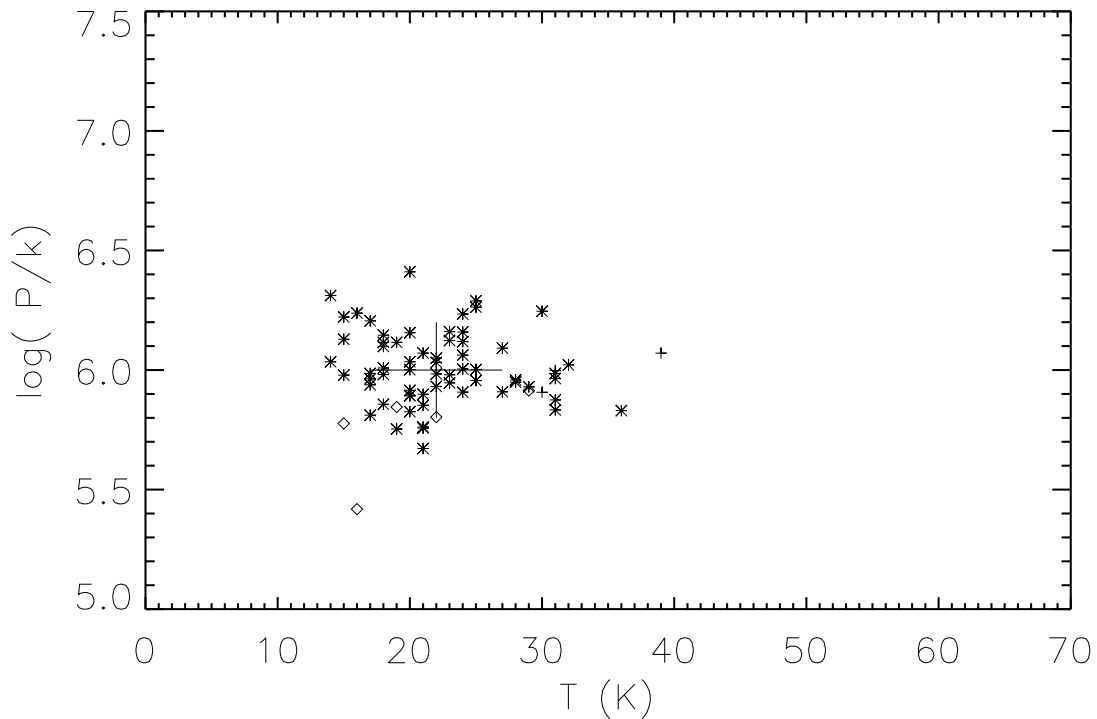


Fig. 6.— Results of determining the physical parameters of clumps using the assumption that they are well represented by Bonnor-Ebert spheres with measured concentrations. Plotted are the external, confining pressure vs. the internal temperature (assuming an equal contribution from turbulent support). The cross represents the mean and standard deviation of the data points. The typical uncertainty in the derived physical parameters of an individual clump is similar to the spread in the distribution of points. The symbols are the same as in Fig. 5.

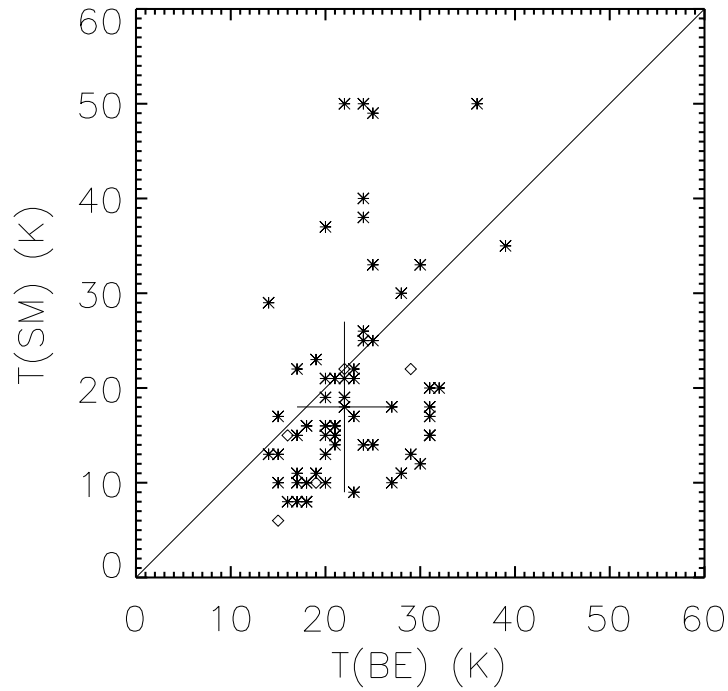


Fig. 7.— Comparison of the clump temperature derived from the Bonnor-Ebert analysis versus the clump temperature derived from spectral energy fitting between the $450\ \mu\text{m}$ and $850\ \mu\text{m}$ observations. A value of 50 K is used to represent sources for which no temperature could be determined from the spectral index. The cross represents the mean and standard deviation of the data points.

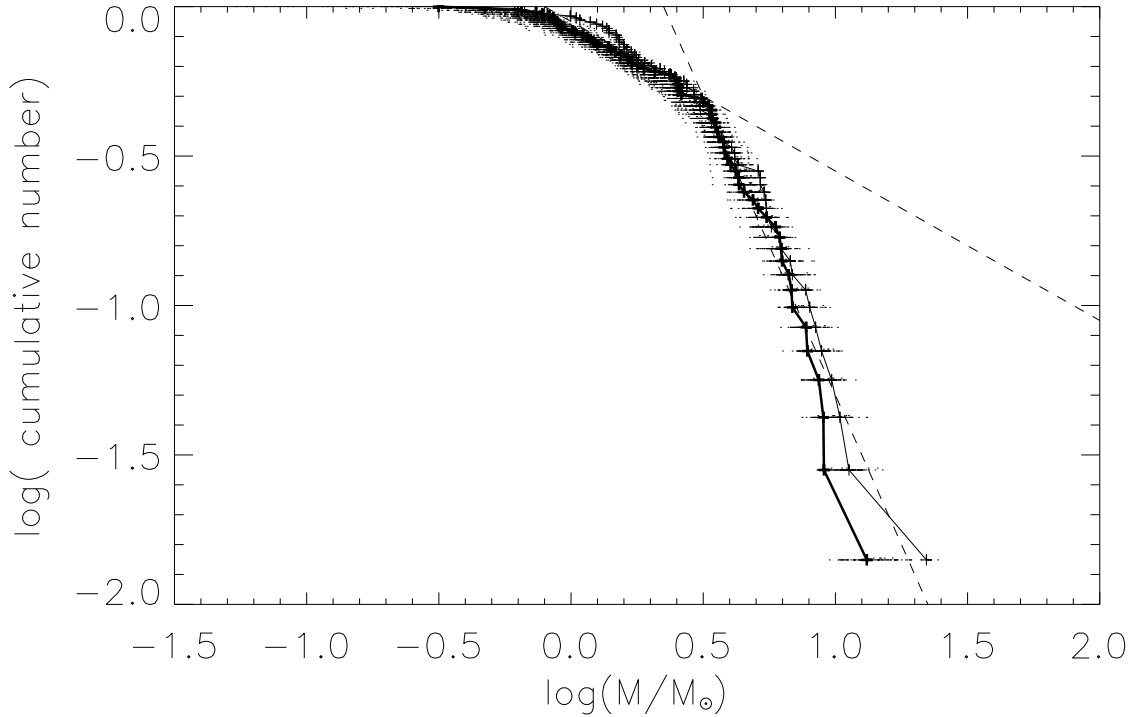


Fig. 8.— Cumulative number function for the $850\ \mu\text{m}$ clumps in Orion A South. The thin line converts the measured flux directly to mass using a constant temperature $T_d = 20\ \text{K}$. The thick line converts the flux to mass using the derived temperature from fitting the clumps to Bonnor-Ebert spheres (see text). The horizontal lines represent the extent to which the masses might change due to one-sigma uncertainties in the Bonnor-Ebert measurements. Since the cumulative mass function depends on the ordering in mass of the clumps, individual points on the horizontal lines were determined by randomly sampling the clump distribution 100 times. The steep dashed line has a slope M^{-2} and approximates the high-mass end of the cumulative distribution. The shallow dashed line has a slope $M^{-0.5}$ and approximates the low-mass end of the distribution. The low-mass end may be severely incomplete (see text).

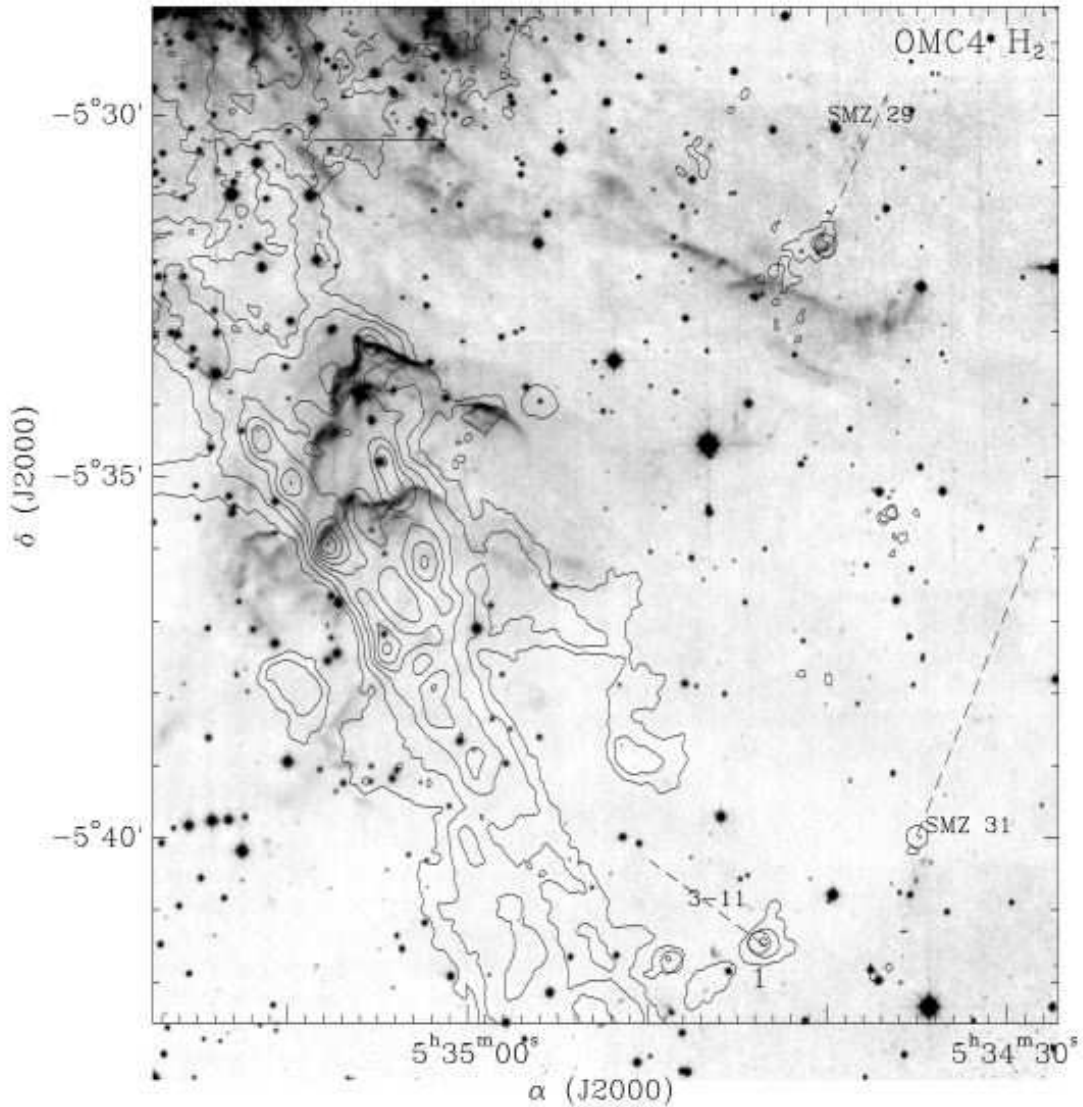


Fig. 9.— The OMC4 region south of the Orion Nebula. Grey-scale shows the H_2 emission from Stanke (2000) and Stanke, McCaughrean, and Zinnecker (2002) overlaid on a contour map of the $850\ \mu\text{m}$ emission. In this and all subsequent figures, contour levels are 100, 200, 400, 600, ... mJy/beam. SCUBA sources are identified by octagons and the ID number. H_2 flows are identified with dashed lines and the SMZ ID.

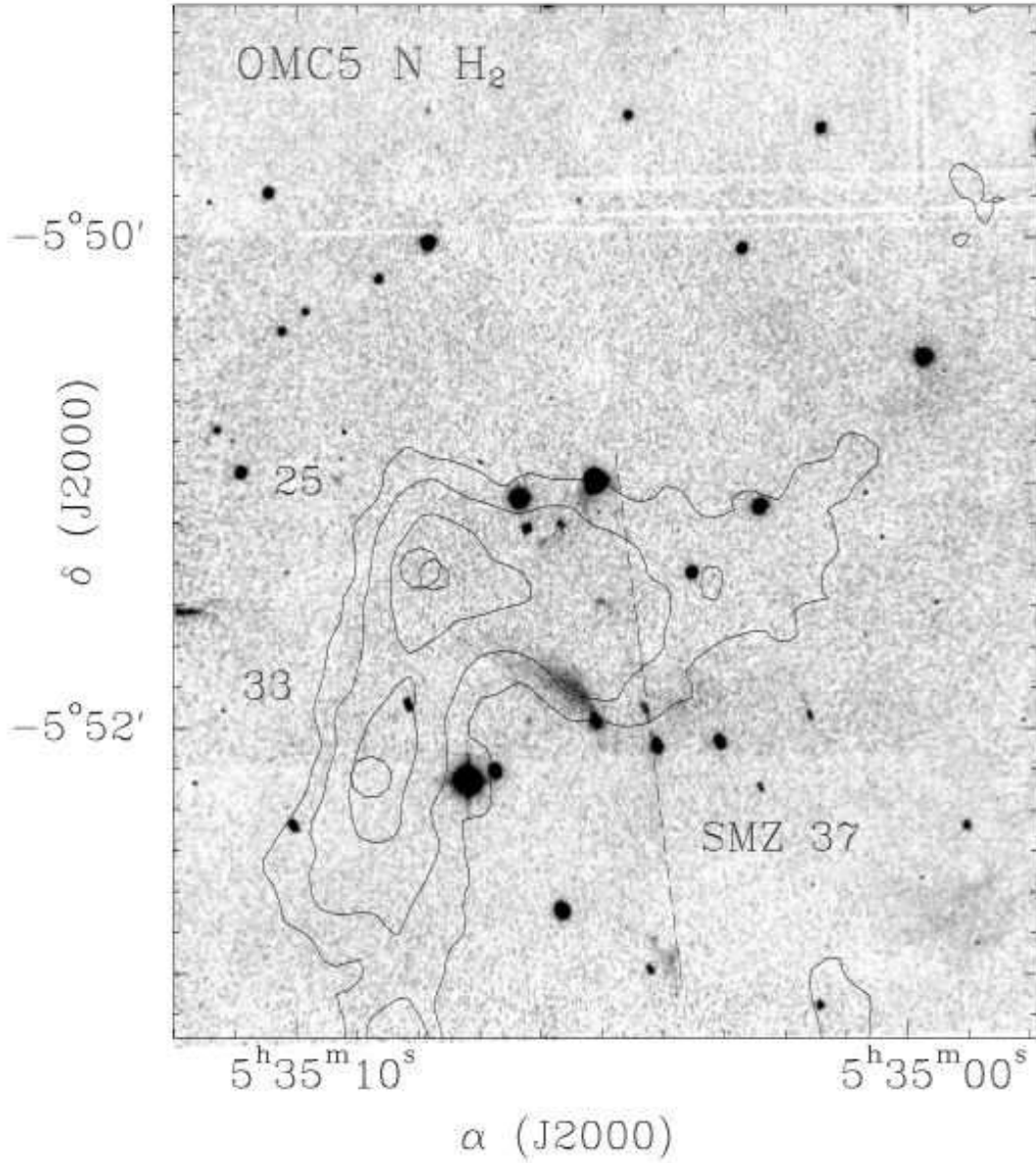


Fig. 10.— A small cluster of SCUBA clumps and H₂ jets at the northern end of the OMC5 region located directly behind the NGC 1980 cluster in Orion.

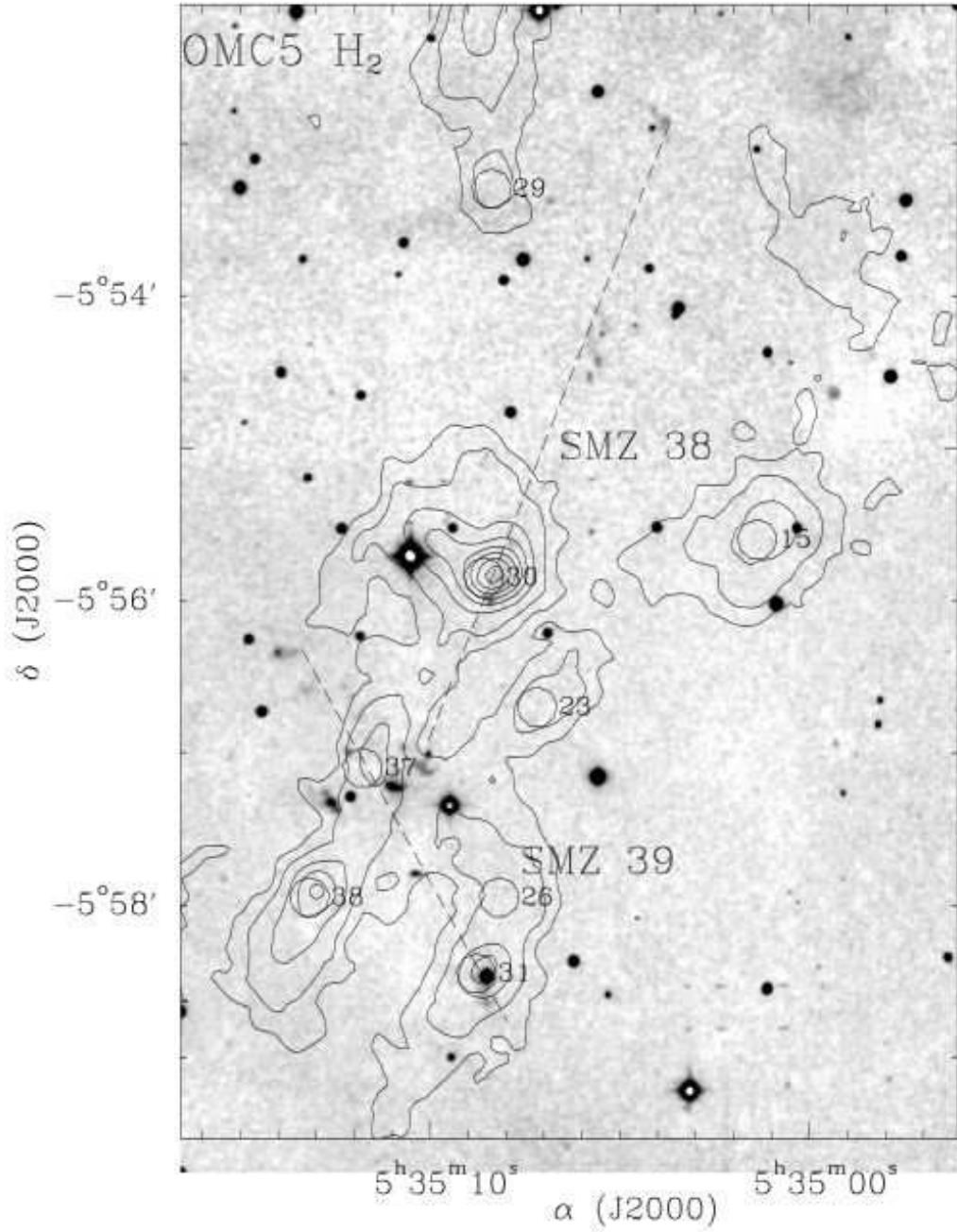


Fig. 11.— The SMZ38 and SMZ39 outflows superimposed on a contour map of the cluster of SCUBA clumps that comprises OMC5 behind NGC 1980.

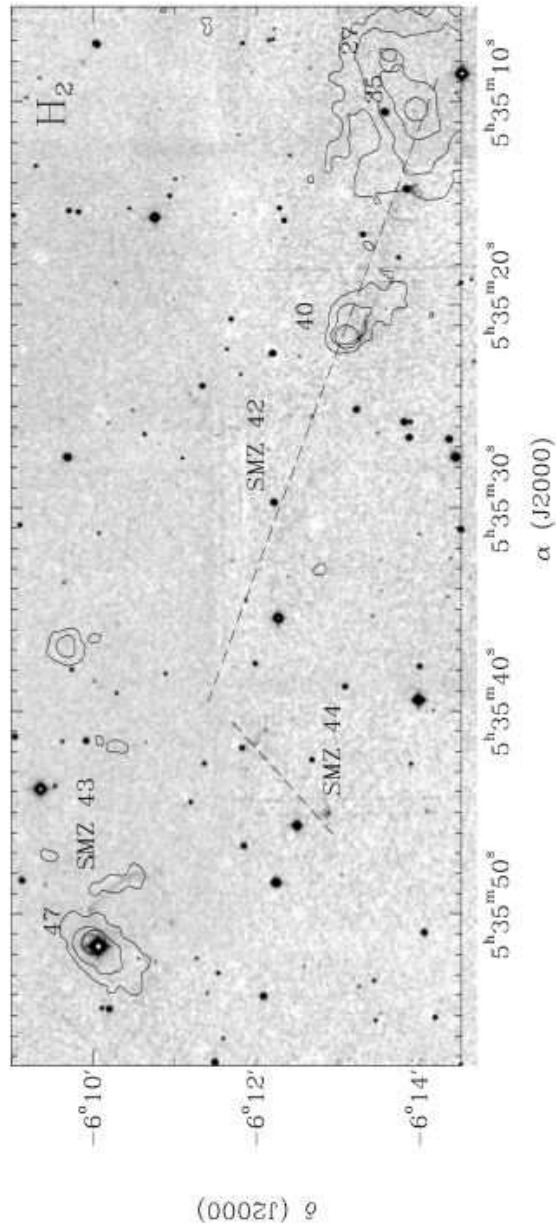


Fig. 12.— H_2 outflows and clumps south of NGC 1980. An H_2 jet (SMZ42) emerges from clump ID 40 in the lower right and drives a giant Herbig-Haro flow towards the south-west (not shown). A pair of H_2 bubbles is associated with clump ID 47 in the upper left (SMZ43).

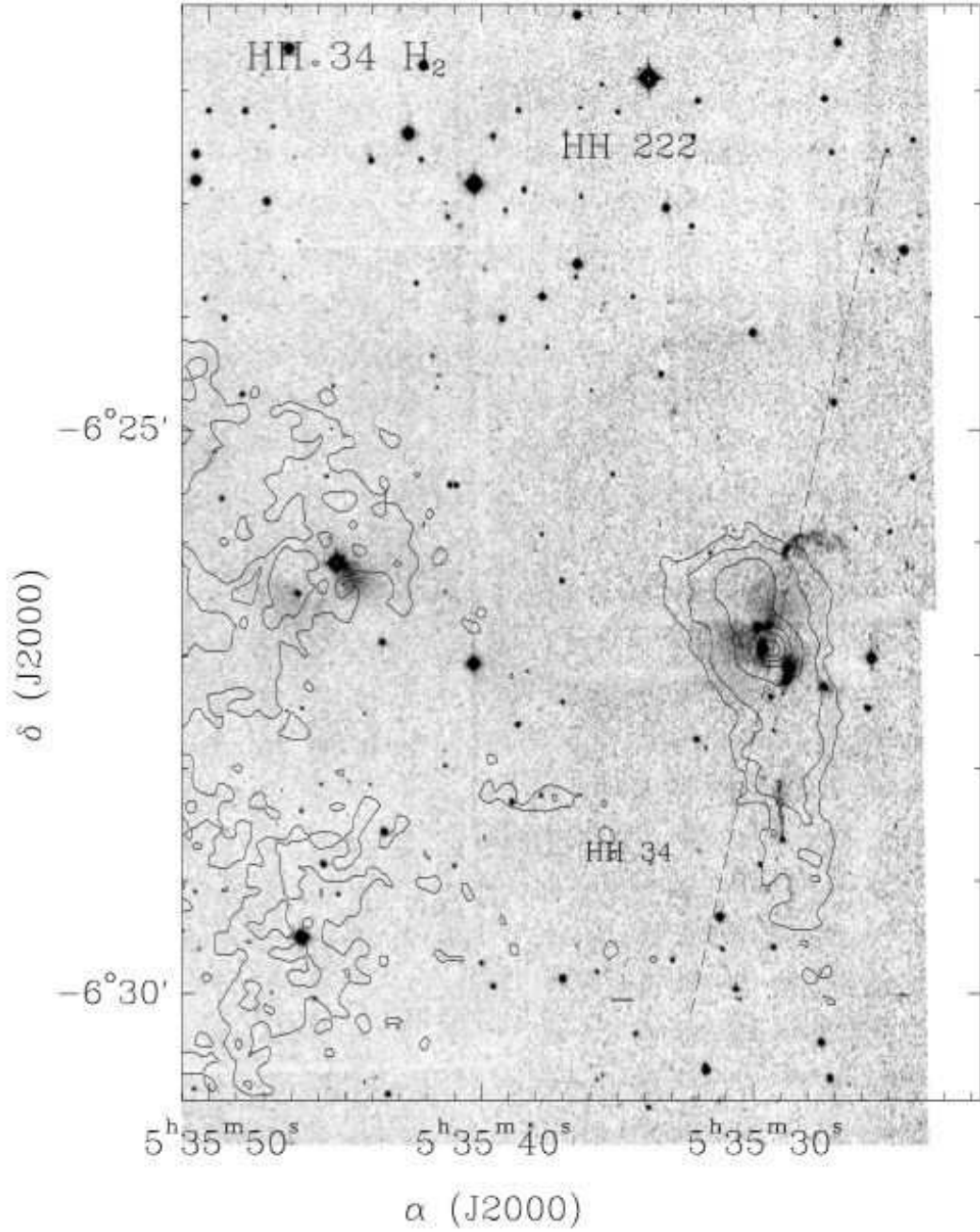


Fig. 14.— The HH 34 region showing H₂ emission and SCUBA contours. SCUBA core ID 41 is the bright peak located on the axis of the HH 34 jet (marked by the dashed line). Core ID 42 is the protrusion that extends about 45'' north-northeast of core ID 41.

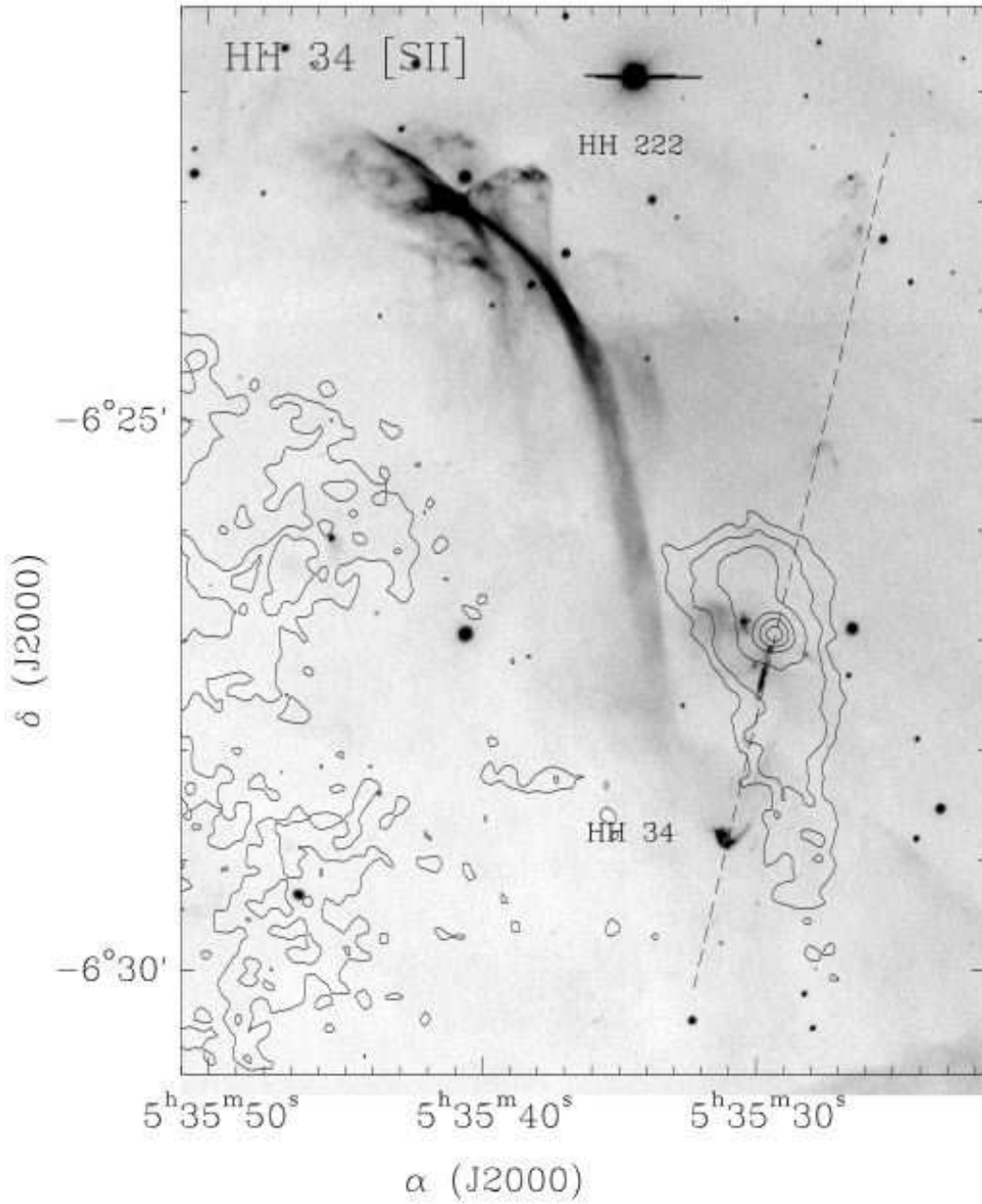


Fig. 15.— The HH 34 region showing [S II] emission and SCUBA contours. SCUBA core ID 41 is the bright peak located on the axis of the HH 34 jet (marked by the dashed line). Core ID 42 is the protosion that extends about $45''$ north-northeast of core ID 41.

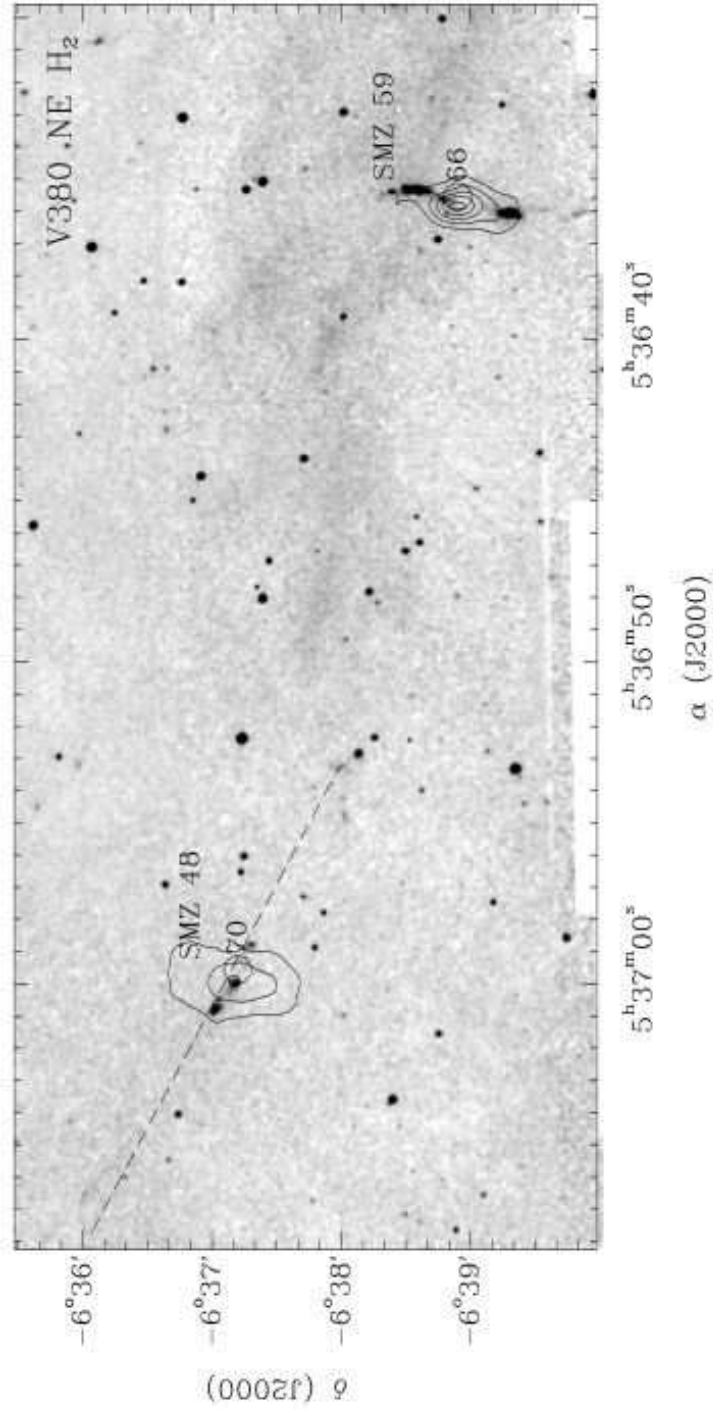


Fig. 16.— The S-symmetric outflow V380 Ori NE emerging from SCUBA clump SMM 053660-06389 (ID 66, lower right). SCUBA clump SMM 053700-06372 (ID 70) drives a larger, but fainter, H₂ outflow (upper left).

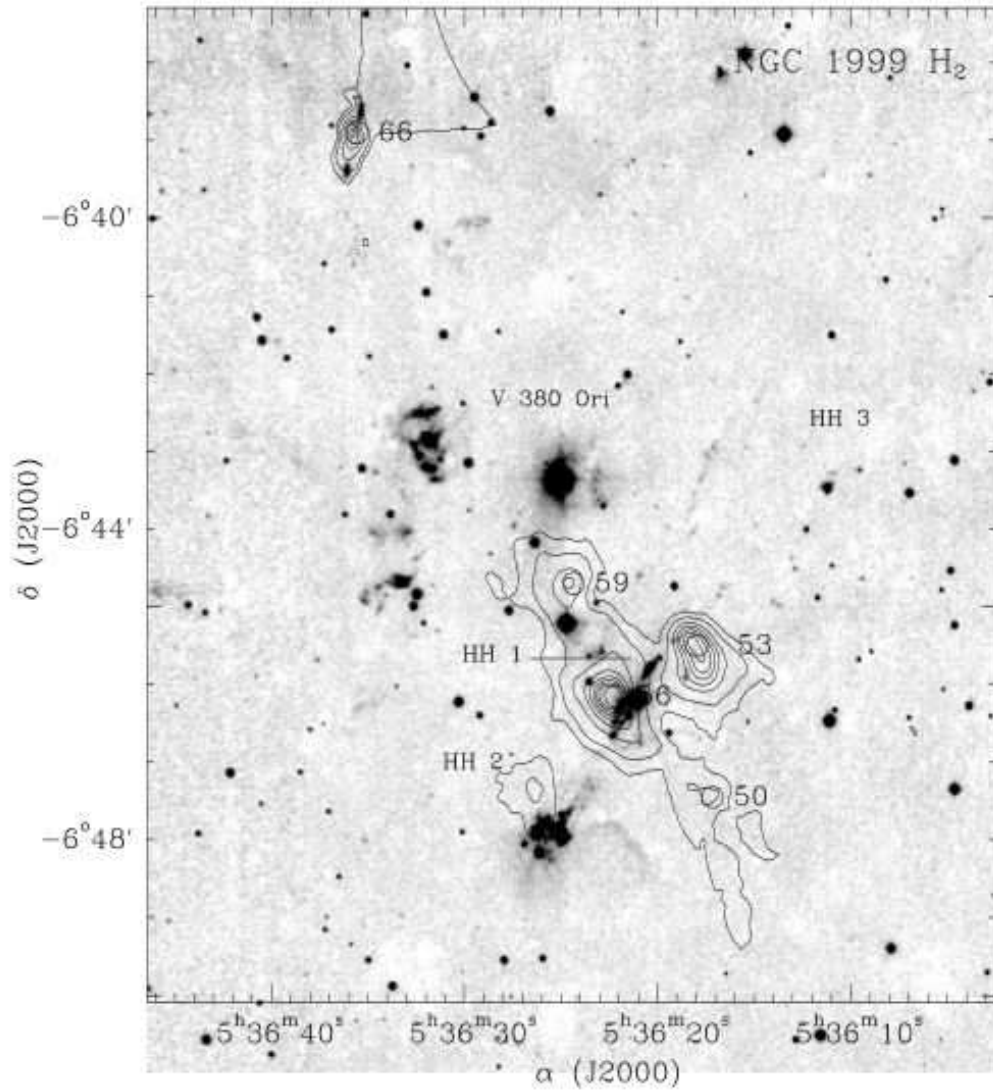


Fig. 17.— The NGC 1999 region containing V380 Ori (IRAS 05339-0644) and the HH 1/2 bipolar outflow emerging from SCUBA clump SMM 053638-06461 (ID 56). SCUBA clump SMM 053631-06455 (ID 53) is associated with an H₂O maser and may be the driver of HH 3 in the upper right of this figure. SCUBA clump SMM 053641-06447 (ID 59) also drives small flow.